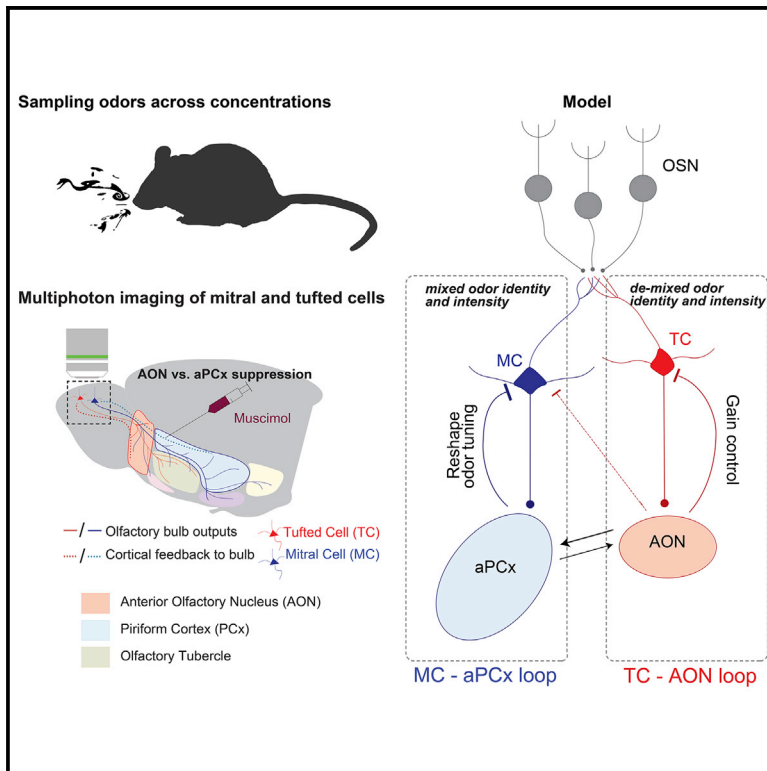# Long-range functional loops in the mouse olfactory system and their roles in computing odor identity

Graphical abstract

Authors

Honggoo Chae, Arkarup Banerjee,
Marie Dussauze, Dinu F. Albeanu

Correspondence

albeanu@cshl.edu

In brief

Chae, Banerjee, et al. identify distinct feedback loops mediated by the mouse olfactory bulb outputs (mitral and tufted cells) and their preferred cortical targets. They suggest that in addition to the mitral-to-piriform cortex pathway, the non-canonical tufted-to-anterior olfactory nucleus pathway is ideally placed for decoding odor identity and intensity.

Highlights

- Mitral and tufted cells form distinct loops with their preferred cortical targets

- Piriform cortex feedback specifically restructures the mitral cell odor responses

- AON feedback controls the gain of tufted cell responses without altering odor tuning

- Tufted cells outperform mitral cells in decoding odor identity and concentration

Neuron

CellPress

Article

Long-range functional loops in the mouse olfactory system and their roles in computing odor identity

Honggoo Chae,[1,3] Arkarup Banerjee,[1,2,3] Marie Dussauze,[1,2] and Dinu F. Albeanu[1,2,4,5,*]

[1]Cold Spring Harbor Laboratory, Cold Spring Harbor, NY, USA
[2]Cold Spring Harbor Laboratory School for Biological Sciences, Cold Spring Harbor, NY, USA
[3]These authors contributed equally
[4]Senior author
[5]Lead contact
*Correspondence: albeanu@cshl.edu
https://doi.org/10.1016/j.neuron.2022.09.005

SUMMARY

Elucidating the neural circuits supporting odor identification remains an open challenge. Here, we analyze the contribution of the two output cell types of the mouse olfactory bulb (mitral and tufted cells) to decode odor identity and concentration and its dependence on top-down feedback from their respective major cortical targets: piriform cortex versus anterior olfactory nucleus. We find that tufted cells substantially outperform mitral cells in decoding both odor identity and intensity. Cortical feedback selectively regulates the activity of its dominant bulb projection cell type and implements different computations. Piriform feedback specifically restructures mitral responses, whereas feedback from the anterior olfactory nucleus preferentially controls the gain of tufted representations without altering their odor tuning. Our results identify distinct functional loops involving the mitral and tufted cells and their cortical targets. We suggest that in addition to the canonical mitral-to-piriform pathway, tufted cells and their target regions are ideally positioned to compute odor identity.

INTRODUCTION

No two stimuli are ever the same. However, the brain readily recognizes different objects in the environment, generalizing under widely varying conditions. For example, humans categorize one person's face as distinct from another, generalizing across differences in viewing angles, brightness, or orientation (DiCarlo et al., 2012). The past decade has seen considerable progress in our understanding of the neural mechanisms underlying visual object recognition (DiCarlo et al., 2012; Hong et al., 2016; Rust and DiCarlo, 2010). Despite recent advances (Bolding and Franks, 2017, 2018; Chae et al., 2019; Pashkovski et al., 2020; Stettler and Axel, 2009), how analogous computations on odorants are supported by specific neural circuits remains an open question.

Two key features of odorants are their identity and intensity. Coffee smells distinct from cheese across most concentrations (logarithmically proportional to the perceived intensity) (Moskowitz et al., 1976; Sirotin et al., 2015). Olfactory behaviors often impose different constraints on decoding sensory representations. For example, while odor identification requires the extraction of response differences across stimuli, generalizing across concentrations of the same odorant necessitates extracting

the common response features. In addition, navigating toward an odor source also requires estimating the relative stimulus concentration and its intermittence (Celani et al., 2014). Although odor discrimination and generalization are key for survival, how these computations are supported by the activity of specific cell types remains unclear.

In mammals, olfactory information is relayed to higher brain regions by two distinct populations of olfactory bulb (OB) output neurons, the mitral cells (MCs) and tufted cells (TCs), which differ in their size, location, intrinsic excitability, local wiring, and activity (Burton and Urban, 2014; Cavarretta et al., 2018; Fukunaga et al., 2012; Geramita and Urban, 2017; Geramita et al., 2016; Gire et al., 2012; Igarashi et al., 2012; Jordan et al., 2018; Kapoor et al., 2016; Nagayama et al., 2004; Otazu et al., 2015; Yamada et al., 2017). MCs and TCs project to approximately a dozen brain regions including the olfactory cortex (anterior olfactory nucleus [AON] and piriform cortex [PCx]) (Shepherd, 1972). TC projections are biased toward the AON and olfactory tubercle ([OT], olfactory striatum) (Igarashi et al., 2012; Nagayama et al., 2010; Shepherd, 2003). Although MCs project widely and strongly innervate the PCx, they send relatively little input to AON (Ghosh et al., 2011; Sosulski et al., 2011). In turn, the AON and the anterior PCx (aPCx), and most other bulb targets, send numerous
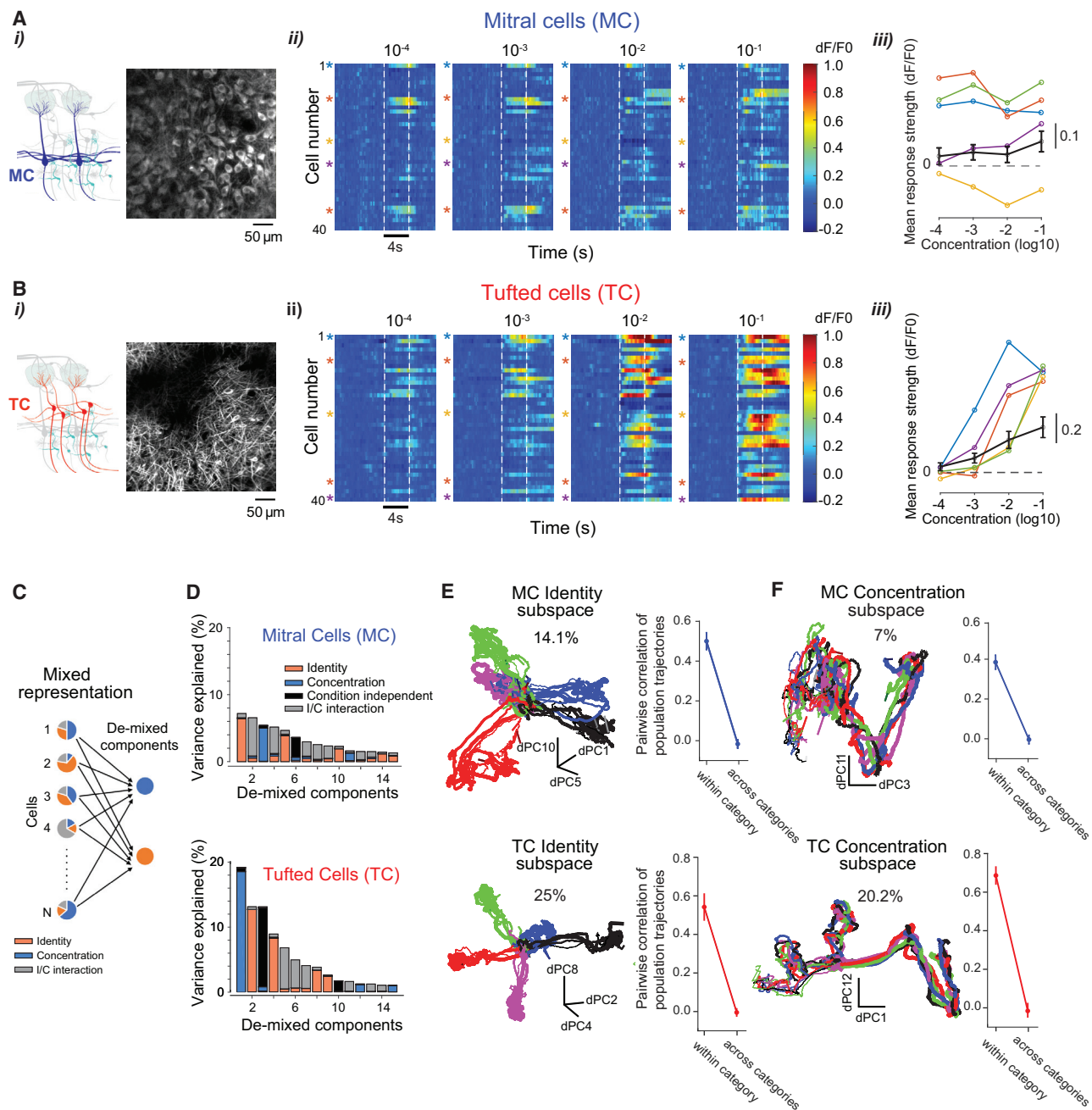
Figure 1. Odor identity and concentration representations in MC and TC ensembles

(A and B) (Ai and Bi) (Left) Cartoon drawing of the olfactory bulb major cell types with MCs (blue, A) and TCs (red, B) highlighted. (Right) Average resting fluorescence of example field of view (FOV) containing MC(A) and TC(B) somata (~225 and 150 μm from surface). (Aii and Bii) Mean peri-stimulus time histogram of simultaneously recorded MC (n = 40, A) and TC (n = 40, B) from two example FOVs to increasing concentrations of valeraldehyde. Color indicates normalized change in fluorescence with respect to pre-odor baseline (dF/F_0). Dotted lines mark odor presentation (4 s). (Aiii and Biii) Mean concentration responses of five example MC (A) and TC (B) indicated by colored fiduciary marks in (Aii) and (Bii). Population responses (black line) were averaged across all MC (n = 40, A) and TC (n = 40, B) in the example FOVs (Ai and Bi).

(C) Cartoon showing that mixed representations of odor identity (orange) and concentration (blue) signals in individual neurons can be linearly "de-mixed" as low-dimensional components of the population activity.

(D) For MC (top) and TC (bottom) ensembles accrued across all fields of view, the variance explained by the top 15 principal components (PCs) identified using demixed-PCA is decomposed into four categories: "identity," "concentration," "interaction between identity and concentration," and "condition independent"; n = 447 MC (5 FOVs, 5 mice) and 458 TC (6 FOVs, 5 mice); stimuli: 5 odors, 4 concentrations.

(legend continued on next page)

Neuron
Article

CellPress

feedback axons that primarily target inhibitory bulbar interneurons (Boyd et al., 2015; Markopoulos et al., 2012; Otazu et al., 2015; Rothermel and Wachowiak, 2014).

Over the past decades, numerous computational models and experimental results (Babadi and Sompolinsky, 2014; Bolding and Franks, 2017, 2018; Choi et al., 2011; Gottfried, 2010; Miura et al., 2012; Roland et al., 2017; Schaffer et al., 2018; Stettler and Axel, 2009; Wilson and Sullivan, 2011) have proposed that intensity invariant odor representations first emerge in the PCx, drawing specifically from MC inputs (Bolding and Franks, 2017, 2018; Miura et al., 2012; Pashkovski et al., 2020; Stettler and Axel, 2009; Wilson and Sullivan, 2011). In contrast to this canonical mitral-to-PCx pathway, the AON, which integrates mainly TC inputs from the bulb (Ghosh et al., 2011; Igarashi et al., 2012; Nagayama et al., 2010; Sosulski et al., 2011), is thought to estimate the location of odor sources by computing the relative stimulus concentration (Esquivelzeta Rabell et al., 2017; Kikuta et al., 2010), processing social cues (Oettl et al., 2016; Wang et al., 2020), and contributing to episodic memory (Aqrabawi and Kim, 2018). The contribution of MCs versus TCs in odor discrimination and generalization across concentrations has been investigated to a much lesser extent. This is partly due to technical limitations of unambiguously differentiating MCs and TCs using extracellular recordings (Bolding and Franks, 2018; Cury and Uchida, 2010; Dhawale et al., 2010; Fantana et al., 2008; Gupta et al., 2015; Li et al., 2015; Wilson et al., 2017). Interestingly, previous studies using whole-cell or juxtacellular recordings showed that TC responses are faster and more robust than MC, which sets them as potential candidates for representing odor identity and intensity (Fukunaga et al., 2012; Igarashi et al., 2012; Jordan et al., 2018; Nagayama et al., 2004). Additionally, cortical bulbar feedback has been proposed to enable the separation of odor representations, sparsening MC responses by targeting specific sets of granule cells which, in turn, inhibit the MCs (Grabska-Barwińska et al., 2017; Koulakov and Rinberg, 2011; Otazu et al., 2015). However, despite overwhelming evidence for massive top-down projections to the bulb and the presence of extensive interactions between olfactory cortical areas (AON versus PCx), the specificity and logic of interplay between feedforward input and cortical bulbar feedback signals acting on the MCs and TCs remain poorly understood.

Here, we took advantage of multiphoton microscopy that affords differentiating between MCs and TCs and monitored their responses to odors in awake mice while varying stimulus concentration. We asked four specific questions. Do MCs and TCs differ in their ability to convey odor identity information? Is cortical feedback from the piriform and AON specific in controlling the activity of their dominant inputs cell types? Does cortical bulbar feedback originating in the piriform versus AON implement different computations? What is the relative contribution

of feedforward versus feedback inputs to supporting the MC and TC representations of odor identity and intensity? Our experiments identified distinct functional feedforward-feedback loops mediated by the MCs and TCs and their preferred cortical targets. They suggest that in addition to the MCs-to-PCx pathway, the non-canonical TCs-to AON pathway is ideally placed for decoding odor identity and intensity.

RESULTS

Representations of odor identity in MC and TC ensembles

We investigated whether odor identity and concentration can be decoded from MC and TC populations and the extent to which this depends on cortical feedback. We recorded the OB output activity in awake head-fixed mice in response to 5 odorants whose concentration was varied across 3 orders of magnitude (GCaMP6f, Table S1, Odor Set A) (Chen et al., 2013), as well as to a 20 odors panel (GCaMP3, Table S1, Odor Set B) (Tian et al., 2009) presented each at a single concentration (STAR Methods; Figures S1A–S1G). Multiphoton imaging of GCaMP3/6f signals enabled us to distinguish MCs versus TCs based on the location of their cell bodies in the OB (Figures 1A, 1B, S1, S4A, and S4B; STAR Methods).

Consistent with previous reports (Chae et al., 2019; Fukunaga et al., 2012; Igarashi et al., 2012; Jordan et al., 2018; Meredith, 1986; Nagayama et al., 2004), we found differences in the mitral and tufted responses to the same stimuli. Notably, MC responses were slow, sparse, and phasic (Figure 1A). Moreover, individual neurons had non-monotonic concentration response curves (Figure 1A) in contrast with previous reports in anesthetized mice (Igarashi et al., 2012; Kikuta et al., 2013). TCs showed fast and sustained responses to odorants (Figures S1B and S1C) whose magnitude increased monotonically with increasing concentration (Figure 1B). Additionally, TC responses were more reliable, displaying lower trial-to-trial variability in comparison to MCs (Figure S1D).

We used de-mixed principal component analysis (dPCA) (Kobak et al., 2016) to investigate whether odor identity and concentration information could be linearly separated from the MC and TC responses (Figures 1C–1F). Success in de-mixing the identity and concentration dimensions implies that a linear combination of neuronal activity can "decode" odor identity with concentration invariance, although a different linear combination of the same neural responses can be used to infer stimulus concentration, irrespective of the odor identity (Figures 1C and 1D). Indeed, we found that odor identity as well as concentration can be de-mixed and linearly read-out using ensemble activity from both MCs and TCs. To quantify this observation, we calculated the pairwise

---

(E) (Left) Population trajectories in the neural state space defined by the top 3 identity PCs from (D). For MCs (top) and TCs (bottom). Different colors denote different odorants, whereas increasing thickness indicates increasing concentration. Total variance explained by the top 3 identity PCs: MC: 14.1%; TC: 25.8%. (Right) Pairwise correlation of population trajectories within category (same odor across concentrations) versus across categories (different odors and concentrations) for MCs (top) and TCs (bottom).

(F) (Left) Same as (E), except that neural trajectories are depicted in the sub-space defined by the top 2 concentration PCs. Total variance explained: MC: 7%; TC: 20.2%. (Right) Pairwise correlation of population trajectories within category (same concentration across odors) versus across categories (different odors and concentrations) for MCs (top) and TCs (bottom).
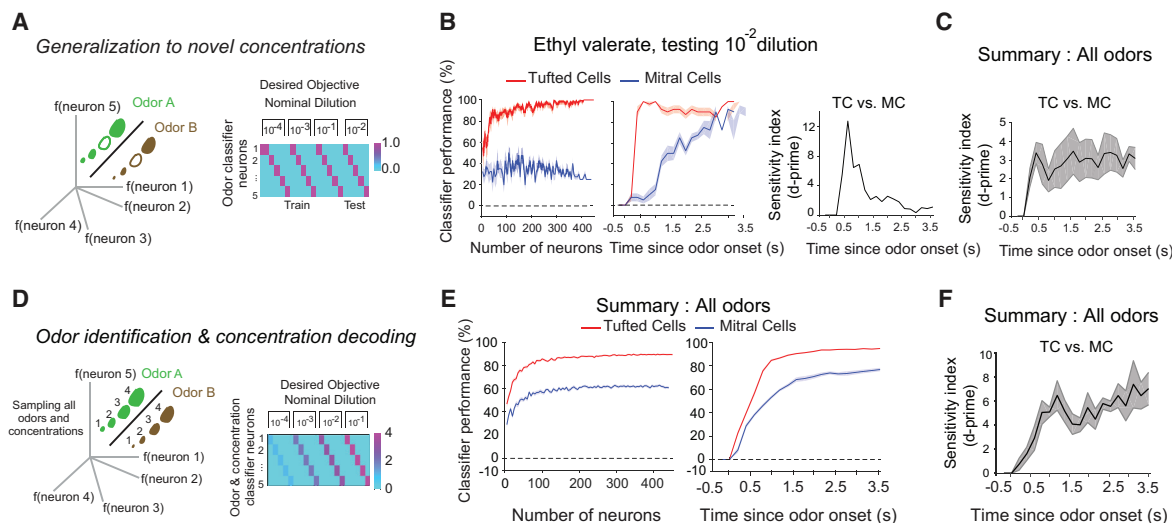
See also Figure S1.

Figure 2. TC ensembles outperform MCs in decoding odor identity and concentration

(A) Generalization across concentrations. (Left) The SVM decoder learns to group together any three of four concentrations sampled for a given odorant. Increasing size of odor representations denotes increasing concentration. Cross-validated performance is tested on the ability to classify the fourth concentration previously not used for training (empty circles). (Right) Setup of the decoding strategy where hypothetical classifier neurons (one for each odor) signal the presence (value = 1) of their corresponding odor for all four sampled concentrations and its absence (value = 0) for all other odors in the panel.

(B) (Left) Cross-validated classification performance of generalization across concentrations for an example odor (ethyl valerate), whereas increasing number of MCs (blue) and TCs (red) at a fixed time point (t = 1 s). (Center) Classification performance for the example odor as a function of time for 200 randomly chosen neurons with bootstrap re-sampling. (Right) TC and MC ensemble performance as quantified by the sensitivity index (d′, d-prime, STAR Methods).

(C) Summary of the difference between MC and TC performance (d-prime) averaged across all odors in the panel. Baseline decoder performance is 0.

(D) Odor identification and concentration decoding. The decoder learns to identify both the odor identity and the relative concentration (on a log scale). Cross-validated performance is evaluated across held-out trials.

(E) (Left) Classification performance averaged across all five odors with increasing number of MCs (blue) and TCs (red) at a fixed time point (t = 1 s). (Right) Classification performance averaged across all five odors as a function of time for 200 randomly chosen MC and TC.

(F) Same as (C), for odor identification and concentration decoding. n = 447 MC (5 FOVs, 5 mice) and 458 TC (6 FOVs, 5 mice); stimuli: 5 odors, 4 concentrations. Time was discretized in 200-ms bins and data plotted such that the decoding performance evaluated from 0 to 0.2 s was plotted in the 0-s bin. Similarly for the rest of the odor period. Shaded areas are SEM unless stated otherwise.

See also Figure S2.

correlation between population trajectories in the neural state space. In the identity sub-space, for both MCs (447 MC, 5 FOVs, 5 mice) and TCs (458 TC, 6 FOVs, 5 mice), the pairwise correlation between population trajectories within category (same odor, across concentrations) was substantially higher than across all trajectory pairs (odors and concentrations); the same was found in the concentration sub-space (Figures 1E and 1F, right). Accumulating across FOVs, the first 3 principal components (PCs) explained 14.1% of signal variance for MC versus 25.8% for TC, suggesting that tufted ensembles were superior to MCs at differentiating odor identity invariant of concentration compared (Figure 1E). Additionally, the first 2 PCs in the concentration sub-space explained 7% of the signal variance for MCs versus 20.2% for TCs, suggesting that TCs are superior to MCs in segregating different odor concentrations (Figure 1F). The degree of de-mixing of olfactory information achieved with this method was substantially larger than by maximizing the overall variance using PCA (Figures S1H and S1I; STAR Methods).

Decoding odor identity with concentration invariance from the OB outputs

We used dimensionality reduction approaches to provide a qualitative intuition for the neural representation of odor identity and concentration. For quantification, throughout the rest of the study, we resorted to cross-validated decoding approaches. To quantify the ability of MC and TC ensembles to perform odor identification, we used linear and non-linear decoding schemes (STAR Methods). Specifically, we analyzed the performance of MCs and TCs in two decoding schemes inspired from analogous computations necessary for solving olfactory behavioral tasks. First, we probed for generalization to a novel concentration, after odor identity was learned from a set of concentrations (Figures 2A–2C, generalization across concentrations). We trained the classifier to identify the odorant (one out of five possibilities) by learning on three of the four concentrations and further tested for generalization to a novel held-out concentration. Identifying a specific odorant across many concentrations is likely to involve such a computation. Second, we aimed to decode both odor identity and concentration, wherein the classifier algorithm (support vector machine [SVM]) was tasked with identifying the presence of the corresponding odorant, as well as simultaneously reporting its relative concentration (Figures 2D–2F, odor identification and concentration decoding; STAR Methods). This second decoding scheme (Figure 2D) is similar to the generalization across concentrations (Figure 2A), except that the classifier neuron for a given

CellPress

odor (e.g., Odor 1) has to fire in proportion (log scale) to concentration without explicitly requiring invariance across concentrations of the same odorant. This computation is likely important for tracking a target odorant along a concentration gradient. By systematically varying the number of cells included in analysis, we trained, evaluated, and cross-validated the decoders' performance at different time points from odor onset (baseline SVM decoder performance is 0, Figures S9D–F).

TCs substantially outperformed MCs in odor generalization across concentrations, both in time and with respect to the number of neurons required for comparable accuracy (earlier and fewer cells, Figures 2B and 2C). We quantified the differences in the TC versus MC performance using a sensitivity index (d′, STAR Methods; Figures 2B and 2C) and found them to be robust and appearing early, within behaviorally relevant timescales (200–500 ms) from odor onset (Figures S1A–S1C). Importantly, small subsets of randomly selected TCs (∼10 cells) were sufficient for successful decoding (Figures 2B and 2E), highlighting the distributed nature of odorant representations. Furthermore, TCs were better also at simultaneously decoding odor identity and concentration compared with MCs (Figures 2D–2F). TC-based decoders were also superior to MC decoders when specifically trained to assign odor identity irrespective of concentration (concentration invariant odor recognition, Figures S2A–S2E and S8A–S8G; STAR Methods).

A potential explanation for the difference in decoding performance of the two cell type ensembles could be technical: MCs are located deeper than TCs, and thus, imaging MC activity is in principle more difficult. Furthermore, TC odor responses are generally higher in amplitude (Figures 1A and 1B). To account for intrinsic differences in response magnitude across MCs and TCs, their activity was Z scored before performing any decoding analyses and found to span the same range (Figures S1E and S1F; STAR Methods). We further analyzed the signal-to-noise ratio (SNR) of MC and TC responses (average signal/standard deviation of signal across individual repeats). We found that the SNR of MC and TC responses is comparable (see largely overlapping distributions, Figure S1G), despite differences in the z axis positions of their somata (slightly higher for TCs versus MCs; median SNR MCs = 3.25; 1,809-cell-odor pairs; median SNR TCs = 4.46; 2,138-cell-odor pairs). The higher decoding performance of tufted versus mitral ensembles we observed is consistent with previous work using electrophysiology measurements that do not suffer from potential methodological SNR differences when sampling MC versus TC responses. These studies found that TCs responses occur substantially earlier and are stronger compared with those of MCs (Fukunaga et al., 2012; Igarashi et al., 2012; Jordan et al., 2018; Nagayama et al., 2004). In addition, for simple binary odor discrimination, the performance of our decoders based on either of the two cell types was high and similar (98% and 95% for TCs versus MCs at 1 s from odor onset), mirroring reports from rodents engaged in odor discrimination behaviors (Uchida and Mainen, 2003; Uchida et al., 2006; Zariwala et al., 2013). Therefore, technical considerations are unlikely to account for the higher decoding performance of TCs compared with MCs.

In summary, TC ensembles appear to carry sufficient information to infer odor identity with concentration invariance, as well as to extract the relative odor concentration, and outperform MC representations to the same stimuli (for further comparison of the decoders performance, see STAR Methods). Taken together with known biases in the projection patterns of MCs versus TCs (Ghosh et al., 2011; Igarashi et al., 2012; Nagayama et al., 2010; Shepherd, 2003; Sosulski et al., 2011), these results suggest that OB target regions other than the PCx, such as the AON and OT, which receive strong TC input, are well positioned to compute odor identity.

Cortical feedback preferentially regulates the activity of its dominant OB input

The responses of MCs and TCs are shaped both by feedforward input from olfactory sensory neurons (OSNs), local interactions via interneurons, as well as top-down feedback from the cortex and other brain regions (Boyd et al., 2015; Kapoor et al., 2016; Markopoulos et al., 2012; Otazu et al., 2015; Rothermel and Wachowiak, 2014; Shepherd, 2003). As a first step toward evaluating how cortical feedback affects the decoding of odor identity and concentration in the bulb outputs, we investigated the specificity of cortical feedback from the PCx and AON in regulating the MC and TC activity. We suppressed the AON or aPCx activity using muscimol (a GABA-A receptor agonist, Figures 3A–3C; STAR Methods) (Otazu et al., 2015) and probed the changes in the odor responses of MCs and TCs. aPCx sends feedback projections only ipsilaterally, whereas the AON feedback projections run bilaterally (Boyd et al., 2012, 2015; Markopoulos et al., 2012; Matsutani, 2010; Shepherd, 2003; Shipley and Adamek, 1984; Figures S3A–S3E). We therefore monitored the change in MC and TC GCaMP3 responses upon inactivation of the ipsilateral aPCx, ipsilateral AON, as well as contralateral AON (Figures 3, 4, and S3A–S3E). To account for potential non-specific decay in responses over long imaging sessions (before and after muscimol/saline injection), all changes in MC and TC activity were normalized to saline regression controls (Figures S4C–S4F, S5, S6B, S6C, and S6F–S6I; STAR Methods).

Consistent with our previous results (Otazu et al., 2015), suppression of the ipsilateral aPCx specifically modulated MC but not TC responses (Figures 3B–3G). Compared with saline injection controls, ipsilateral aPCx suppression increased MC responsiveness (response amplitude and frequency, Figures 3D–3G) as well as the pairwise similarity in MC odor representations (odor similarity, Figures 4A–4C and S5A–S5E; STAR Methods). TC responses were largely unaffected by the suppression of the aPCx (Figures 3D–3G). Conversely, suppression of the ipsilateral AON had substantially stronger impact on TCs compared with MCs. Ipsilateral AON suppression resulted in increased amplitude and number of TC responses (Figures 3D–3G and S4C–S4F) and higher pairwise odor similarity (Figures 4A–4C, S5D, and S5E). The preferential modulation of TCs upon AON suppression was even more apparent upon contralateral AON suppression. Contra-AON suppression had a negligible effect on MCs and specifically boosted individual responsiveness (Figures 3D–3G and S4C–S4F) and pairwise odor similarity in TCs (Figures 4A–4C, S5D, and S5E). The higher specificity of contralateral versus ipsilateral AON feedback in regulating TC activity can be explained by the
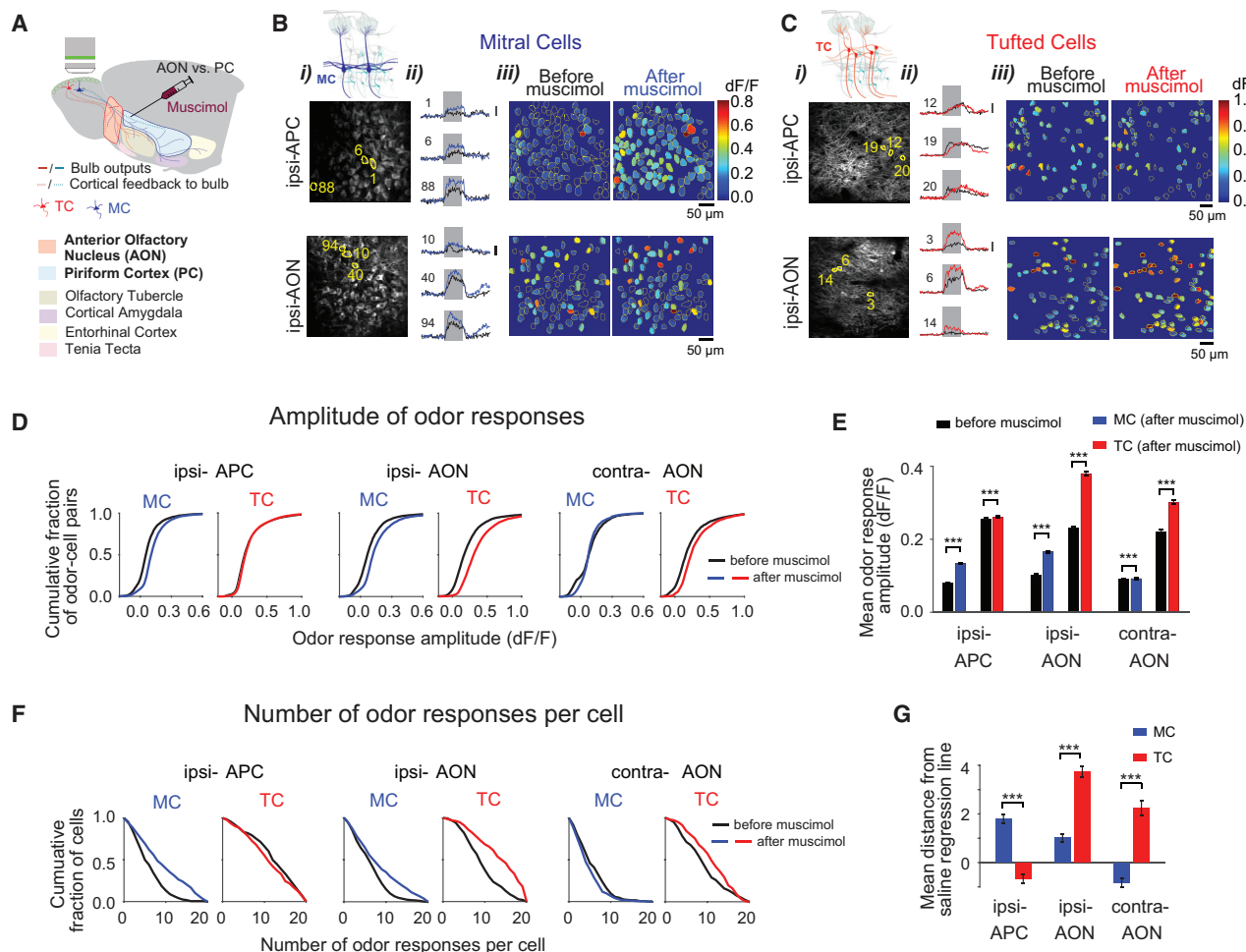
Figure 3. Feedback from the aPCx and AON to the OB preferentially regulates the odor responsiveness of MCs versus TCs, matching biases in feedforward connectivity

(A) Schematic of experimental procedures: cartoon representation of the OB and its major projection targets including the AON, PCx, OT, cortical amygdala, lateral entorhinal cortex, and tenia tecta. Dotted lines indicate cortical feedback to OB from the PCx and AON. MC and TC odor responses were sampled in awake head-fixed mice via two photon imaging of GCaMP3/6f signals before and after suppression of activity in the aPCx and AON, respectively, via muscimol injection.

(B and C) (Top, left) Cartoon drawing of the OB major cell types with MCs (blue) and TCs (red) highlighted. Two example fields of view (220 and 150 μm below the surface) of MCs (B) and TCs (C). The marked cells (left, Bi and Ci) match the example traces shown (center, Bii and Cii); gray shaded area marks odor duration. The traces (center, Bii and Cii) represent the change in fluorescence (dF/F_0) to odor stimulation before- (black) and after-muscimol suppression (color) of cortical activity for the MC and TC outlined in (Bi) and (Ci). (Right, Biii and Ciii) Example average odor responses (dF/F_0) to valeric acid of MCs (rightmost columns, B) and TCs (rightmost columns, C) in the two example fields of view before (left) and after (right) muscimol injection into aPCx (top, ipsi-aPCx) and AON (bottom, ipsi-AON).

(D) Cumulative distribution of MC and TC odor response pairs as function of dF/F_0 response amplitude before (black) and after (blue: MC, red: TC) muscimol injection into ipsi-aPCx, ipsi-AON, and contra-AON.

(E) Summary of mean MC and TC odor response amplitude (dF/F_0, cell-odor pairs) before (black) and after (blue: MC, red: TC) muscimol injection into ipsi-aPCx (MC: n = 4,682 cell-odor pairs, 5 FOVs, 4 mice, TC: n = 4,316 pairs, 5 FOVs, 4 mice), ipsi-AON (MC: n = 3,971 pairs, 4 FOVs, 4 mice, TC: n = 3,777 pairs, 4 FOVs, 4 mice), and contra-AON (MC: n = 1,656 pairs, 3 FOVs, 3 mice, TC: n = 1,861 pairs, 3 FOVs, 3 mice), ***p < 0.001, one-sided Wilcoxon sign-rank test.

(F) Cumulative distributions of number of odors in the panel that individual MC and TC responded to before (black) and after (MC: blue, TC: red) muscimol injection into ipsi-aPCx, ipsi-AON, and contra-AON.

(G) Summary of mean distance from saline regression line for changes in the number of odor responses per cell after muscimol (blue: MC, red: TC) into ipsi-aPCx, ipsi-AON, and contra-AON. ***p < 0.001, Wilcoxon rank-sum test; also see Figures S3, S4, and S6, Table S2, and STAR Methods. Error bars are SEM unless stated otherwise.

fact that the AON provides substantial input to the ipsilateral (but not contralateral) anterior portion of the PCx (see Discussion). Qualitatively, we observed the same results when responses were compared within individual FOVs (Figures S6A–S6C), as well as for matched sample sizes of MCs and TCs (Figures S6D–S6I).

Taken together, our results indicate that the PCx and the AON exert preferential suppression and decorrelation of the MC and
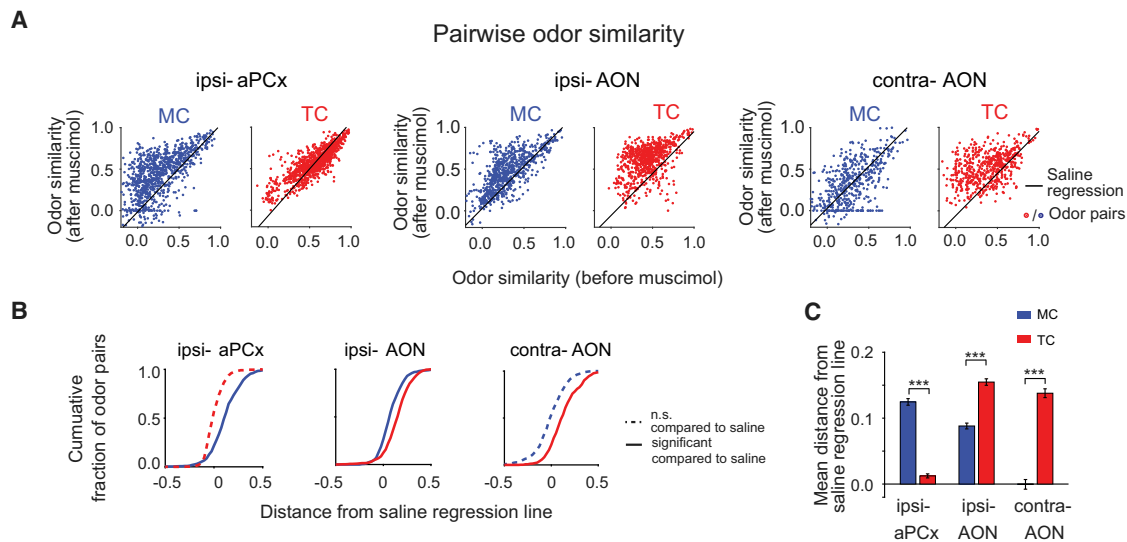
Neuron
Article

CellPress

Figure 4. Feedback from the aPCx and AON to the OB differentially regulates the pairwise correlations of odor representations in MCs versus TCs

(A) Scatter plots of pairwise odor similarity of MC (blue) and TC (red) responses before and after muscimol injection into ipsi-aPCx, ipsi-AON, and contra-AON; each dot represents one odor-to-odor comparison before and after muscimol injection; odor pair comparisons are summed across fields of view (ipsi-aPCx MC: n = 950 pairs, 5 FOVs, 4 mice, TC: n = 950 pairs, 5 FOVs, 4 mice; ipsi-AON MC: n = 760 pairs, 4 FOVs, 4 mice, TC: n = 760 pairs, 4 FOVs, 4 mice; contra-AON MC: n = 570 pairs, 3 FOVs, 3 mice, TC: n = 570 pairs, 3 FOVs, 3 mice).

(B) Cumulative plots of distance distributions from saline regression of MC (blue) and TC (red) odor similarity distributions after muscimol injection into ipsi-aPCx, ipsi-AON, and contra-AON.

(C) Summary of mean distance from saline regression line for pairwise odor similarity of MC (blue) and TC (red) representations before and after muscimol injection into ipsi-aPCx, ipsi-AON, and contra-AON. ***p < 0.001, Wilcoxon rank-sum test. Error bars are SEM unless stated otherwise.

See also Figure S5.

TC activity, respectively. This selectivity in feedback regulation of the two OB output channels mirrors the biases in their feedforward connectivity (Ghosh et al., 2011; Igarashi et al., 2012; Nagayama et al., 2010; Shepherd, 2003; Sosulski et al., 2011), thus revealing the existence of two long-range functional loops that may serve different computations.

Differential effects of the cortical feedback on the MCs versus TCs

How does the cortical feedback change the ensemble OB output? One possibility is that feedback from the anterior PCx and the AON controls the gain of the bulb outputs. If this were true, we expect a scaling of the odor response amplitudes upon cortical inactivation, although largely preserving the odor tuning of individual neurons. Alternatively, cortical feedback may provide specific information and restructure the population activity, acting beyond simple scaling of response amplitude.

aPCx suppression increased the response probability of MCs, rendering them responsive to odors in the panel, which did not evoke a significant response before aPCx silencing (Figures 5A and 5D, black and blue). In contrast, the odor responses of TCs remained similar before versus after AON silencing, consistent with a gain control scenario (Figures 5B and 5E, black and red). To quantify this observation, for each cell type and site of inactivation, we analyzed the changes in the odor response tuning of individual cells (Figures 5A–5C), as well as the changes in

cell responses to a given odor (Figures 5D–5I) before versus after muscimol injection.

Briefly, for each neuron, we constructed a vector that represents its mean response magnitude to our panel of 20 odorants (GCaMP3, Table S1, Odor Set B). We computed the correlation (uncentered correlation coefficient, STAR Methods) between the response vectors before versus after muscimol application. Scaled-up responses after muscimol (gain control model) would lead to very similar odor response vector "shapes" and result in correlation values close to 1. In contrast, re-structured neural activity would correspond to different odor response vectors and thus to significantly lower correlation values. The analysis showed a substantial difference between individual MCs and TCs. TC odor response vectors were significantly more similar before and after muscimol suppression (of ipsilateral or contralateral AON) with a distribution of correlation values close to 1 (mean 0.95 ± 0.003). In comparison, MC responses before and after muscimol suppression of ipsi-aPCx were different, and the correlations were significantly lower (mean 0.71 ± 0.027), consistent with our hypothesis (Figure 5C).

We also computed the correlation between the cell response vectors to the same odor before and after cortical inactivation and reached the same conclusions (Figures 5D–5H) both when analyzing independently each FOV (Figure 5F), as well as when accumulating responses across FOVs (Figures 5H and S7A). We verified that the differential effect on MC versus TC ensembles was specific to the drug condition and absent in saline
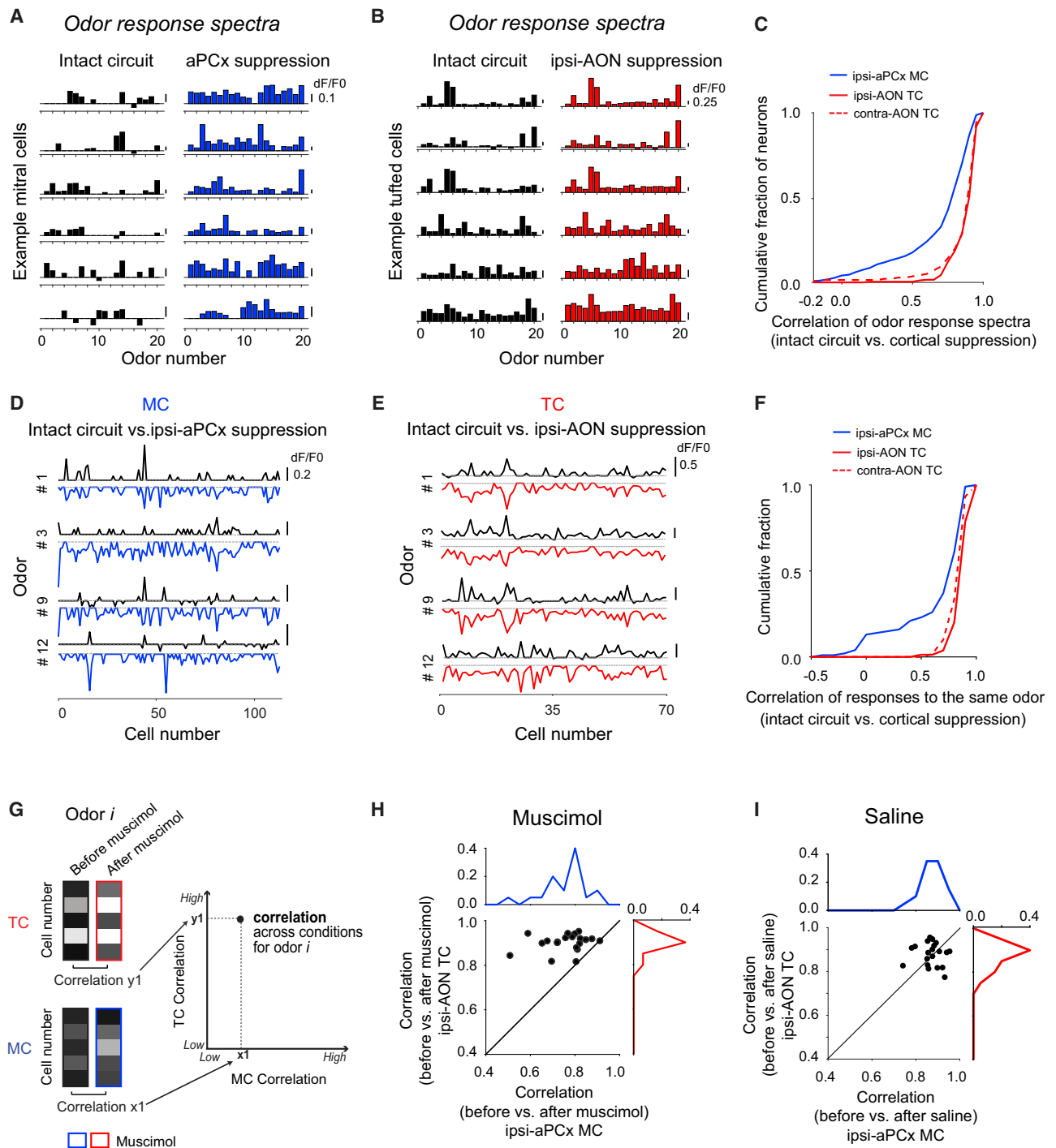
Figure 5. Cortical feedback controls the gain of TC odor representations and restructures MC responses beyond simple scaling

(A and B) Odor response spectra of example MCs (A) and TCs (B) before (black) and after (blue/red) muscimol suppression of ipsi-aPCx (blue) or ipsi-AON (red) activity. Non-significant responses were set to zero for visualization purposes.

(C) Cumulative distributions of correlation of odor response spectra of individual MCs (blue) and TCs (red) before versus after suppression of aPCx (blue) or ipsi-AON (red, solid line) or contra-AON (red, dashed line) activity.

(D) MC response spectra from one field of view to example odors before (upward, black) and after suppression of aPCx (downward, blue).

(E) Same as (D) for TC response spectra before (upward, black) and after suppression of ipsi-AON (downward, red).

(F) Cumulative distributions of correlation of MCs (blue) and TCs (red) responses to individual odors before versus after suppression of ipsi-aPCx (blue, 5 FOVs, 4 mice), ipsi-AON (red solid line, 4 FOVs, 4 mice), or contra-AON (red dashed line, 3 FOVs, 3 mice) activity. Correlation is calculated for each FOV independently.

(legend continued on next page)

Neuron
Article

CellPress

control experiments (Figure 5I). Indeed, when comparing the similarity in cell response spectra for each odor before and after injection of saline (Figure 5I), both TC and MC response correlation distributions were very high, indicating no change in their odor tuning upon injection of saline. The effect on the MC response similarity could not be explained by the overall increase in response amplitude after cortical inactivation. In particular, we asked whether scaling down the post-muscimol responses by a gain factor can account for the effect of muscimol suppression of cortical activity on TC versus MC responses (gain control model). For each cell type, the post-muscimol responses were scaled down (independently for each odor), so as to match the average odor response strength of the distribution of pre-muscimol responses. We found that the correlation between the scaled-down post-muscimol responses and the pre-injection MC responses did not increase (Figures S7B–S7D). Therefore, factors other than simply scaling up the responses (gain control) appear to be at play in shaping the post-muscimol responses of the MCs. In comparison, when the same analysis was performed for the TCs, the correlation coefficients stayed high (Figures S7B–S7D; STAR Methods), consistent with our gain control hypothesis.

Taken together, we find that the cortical target of each OB output cell type predominately controls the activity of its own major input. Furthermore, the net effect of top-down feedback originating in AON versus the anterior PCx appears to differ in regulating the activity of TCs versus MCs. AON feedback regulates the gain of TC responses without substantially changing their odor tuning. In contrast, the effect of anterior PCx feedback is to restructure the MC odor representations beyond simply scaling their response amplitude (Otazu et al., 2015).

Different impact of cortical feedback on decoding of odor identity and concentration by MCs and TCs

Since our experiments measure the activity of the same cells before and after cortical suppression, we investigated whether decoding odor identity and/or concentration (Figures 1 and 2) requires cortical feedback from the aPCx or AON. For both decoding schemes considered (generalization across concentrations and odor identification and concentration decoding), suppressing cortical activity reduced the overall decoding performance for both tufted and mitral ensembles (Figures 6A–6H). However, the drop in performance was substantially smaller for the TCs (when inactivating AON) compared with MC-based decoders (when inactivating aPCx), as quantified using both d' and a performance difference index (difference between the mean classification performance before versus after cortical suppression normalized by their sum, STAR Methods; Figures 6D and 6H). Similarly, a stronger impact of cortical feedback on the MCs

compared with TCs' performance was observed when decoders were specifically trained to assign odor identity irrespective of stimulus concentration (odor recognition, Figures S8A–S8H). In the presence of piriform feedback, the performance of MC-based decoders was significantly higher compared with when piriform activity was suppressed; importantly, the performance of MC-based decoders in the intact circuit was lower than that of TC-based classifiers even after AON suppression. These results suggest that TC ensembles can be used to simultaneously decode odor identity, as well as stimulus concentration using predominantly feedforward processing.

Animals often sample and discriminate between several odor sources in the same sensory scene. To investigate the performance of MC and TC ensembles under more naturalistic conditions, we trained classifiers to perform binary odor discriminations of a target odorant from an increasing number (1–19) of non-target odorants (STAR Methods; Figures 7A–7E). For discrimination involving only two odorants (one target versus one non-target odor), the ensemble tufted as well as mitral cell decoding accuracy reached 95% within 300–400 ms (Figures 7B and 7C). Increasing the number of non-target odorants led to a gradual drop in the TC classification accuracy and an increased latency to reach the same performance criterion (Figures 7B–7E). In comparison, MC decoders were slower and fared poorer in discriminating the target odor from non-targets, across the range of discrimination difficulty tested (Figures 7B–7E). The difference in classification performance between MCs and TCs progressively increased with increasing number of distractor odorants (Figures 7C–7E). Moreover, over this range, the relative impact of cortical feedback was substantially higher for the MCs compared to TCs (Figures 7B, 7E, bottom, and 7D, center, right).

We verified that the decoding performance of TCs cannot be attributed simply to their relative higher response amplitude or to SNR differences compared with MC ensembles (Figures S1B–S1D, S8I, and S9; STAR Methods). The superior performance of TC- versus MC-based decoders did not depend upon the specifics of the decoders employed and was consistent across all decoding schemes investigated (Figures 2, 6, 7, S2, and S8).

DISCUSSION

We investigated whether key odorant features such as identity, concentration, as well as concentration invariant identity can be decoded from the two OB output cell types, and the degree to which the decoding efficiency depends upon cortical feedback from their major targets (PCx and AON). Distinct separation of the OB outputs into MCs and TCs is a feature of land

(G) Cartoon schematics of calculating the correlation of MC (top) and TC (bottom) responses to a given odor in the panel (Odor *i*) before versus after suppression of cortical activity (aPCx or AON).

(H) Scatter plot and histograms of the correlation of responses to individual odors before and after ipsi-aPCx suppression for mitral ensembles (blue, 5 FOVs, 4 mice) and after ipsi-AON suppression for TCs (red, 4 FOVs, 4 mice). Each data point corresponds to correlation of responses to one odor before and after muscimol, accrued across FOVs.

(I) Same as (H), but for saline injection into ipsi-aPCx (4 FOVs, 3 mice) and ipsi-AON (3 FOVs, 3 mice). No thresholding was applied for the analyses in (C), (F), (H), and (I).
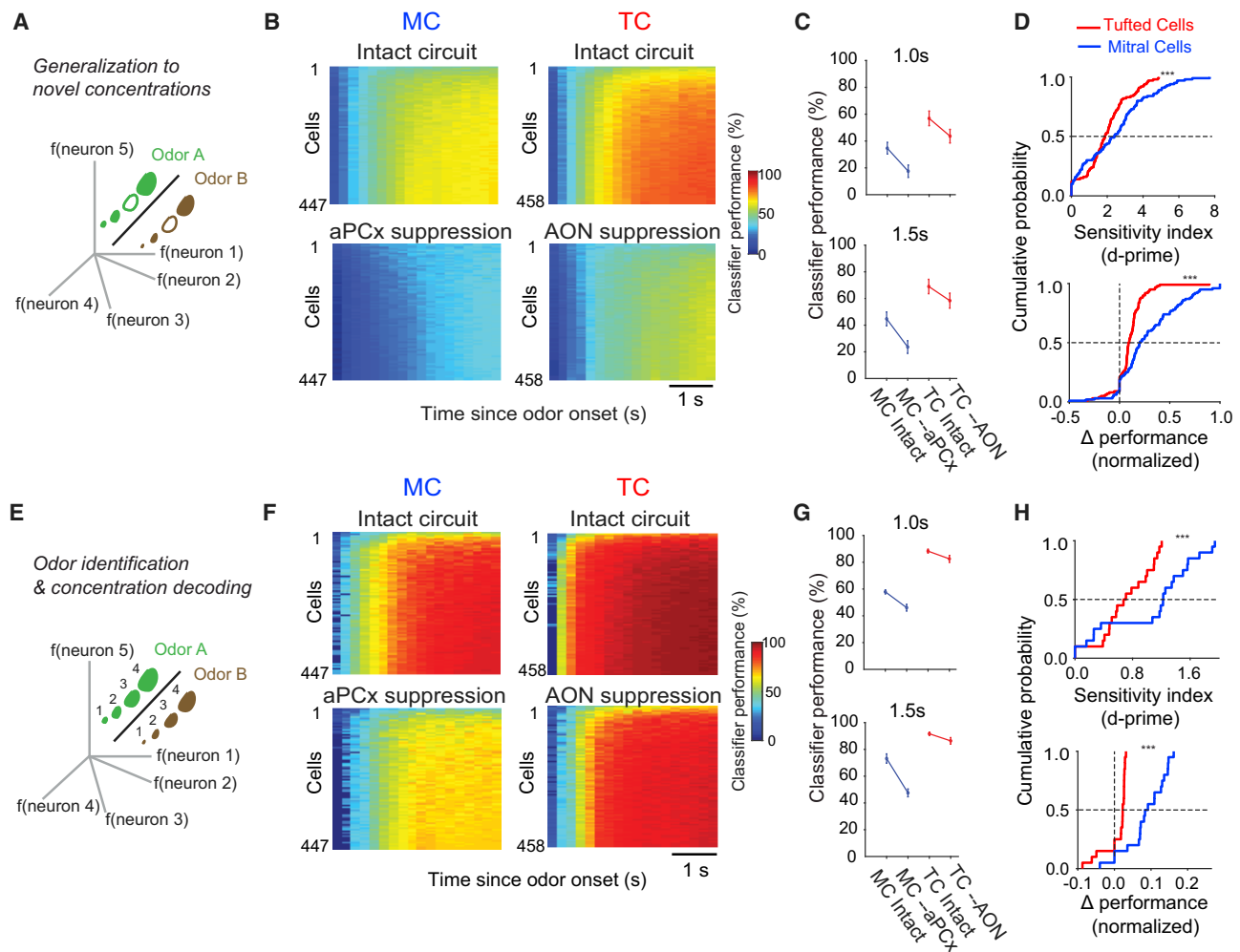
See also Figure S7.

Figure 6. TC ensembles-based decoders of odor identity and concentration outperform MC-based decoders that also depend more heavily on cortical feedback

(A) Generalization to a novel concentration (same as Figure 2A).

(B) 2D decoder performance map (SVM, non-linear) as function of time (abscissa, bin size = 200 ms) while varying the number of neurons included in the analysis (ordinate, bin size = 5) for MCs (left, 5 FOVs, 5 mice) and TCs (right, 6 FOVs, 5 mice) in the presence (top) and after suppressing feedback (bottom) from the preferred cortical target (aPCx for MCs and AON for TCs).

(C) Classifier performance (Avg. ± 95% confidence interval) evaluated at two time points (1.0 and 1.5 s) for the MC- (blue) and TC- (red) based decoders.

(D) Summary of the generalization to novel concentrations decoding scheme: for both MCs (blue, 5 FOVs, 5 mice) and TCs (red, 6 FOVs, 5 mice), classifier performance difference with and without cortical feedback is quantified using d-prime or a performance difference index (Δ performance normalized, STAR Methods). *** indicates $p < 0.001$, paired t test.

(E) Cartoon schematics for the odor identification and concentration decoding (same as Figure 2D).

(F–H) Same as (B–D), respectively, for odor identification and concentration decoding.

See also Figures S8 and S9.

vertebrates, largely absent in fish and amphibians (Andres, 1970), which appears correlated with the emergence of paleo-cortex. Over the past decades, experimental work and computational models have proposed that decoding of odor identity (independent or not of intensity) is a central function of the PCx which is strongly innervated by MCs (Bolding and Franks, 2018; Pashkovski et al., 2020; Stettler and Axel, 2009; Wilson and Sullivan, 2011). The recurrent architecture of the PCx is thought to reformat the MC input so as to generate concentration invariant odor identity representations (Bolding and Franks,

2017; Stettler and Axel, 2009). We found that the TCs, acting to a substantial degree in a feedforward manner, outperform MCs in decoding both odor identity and concentration (Figures 1, 2, 6, and 7). Cortical feedback signals from the PCx and AON preferentially regulate the activity of MCs versus TCs, respectively, matching biases in feedforward connectivity and perform different roles (Figures 3, 4, and 5). Piriform feedback specifically restructures MC responses, while feedback from the AON preferentially controls the gain of TC representations without substantially altering their odor tuning (Figure 8). Overall, the
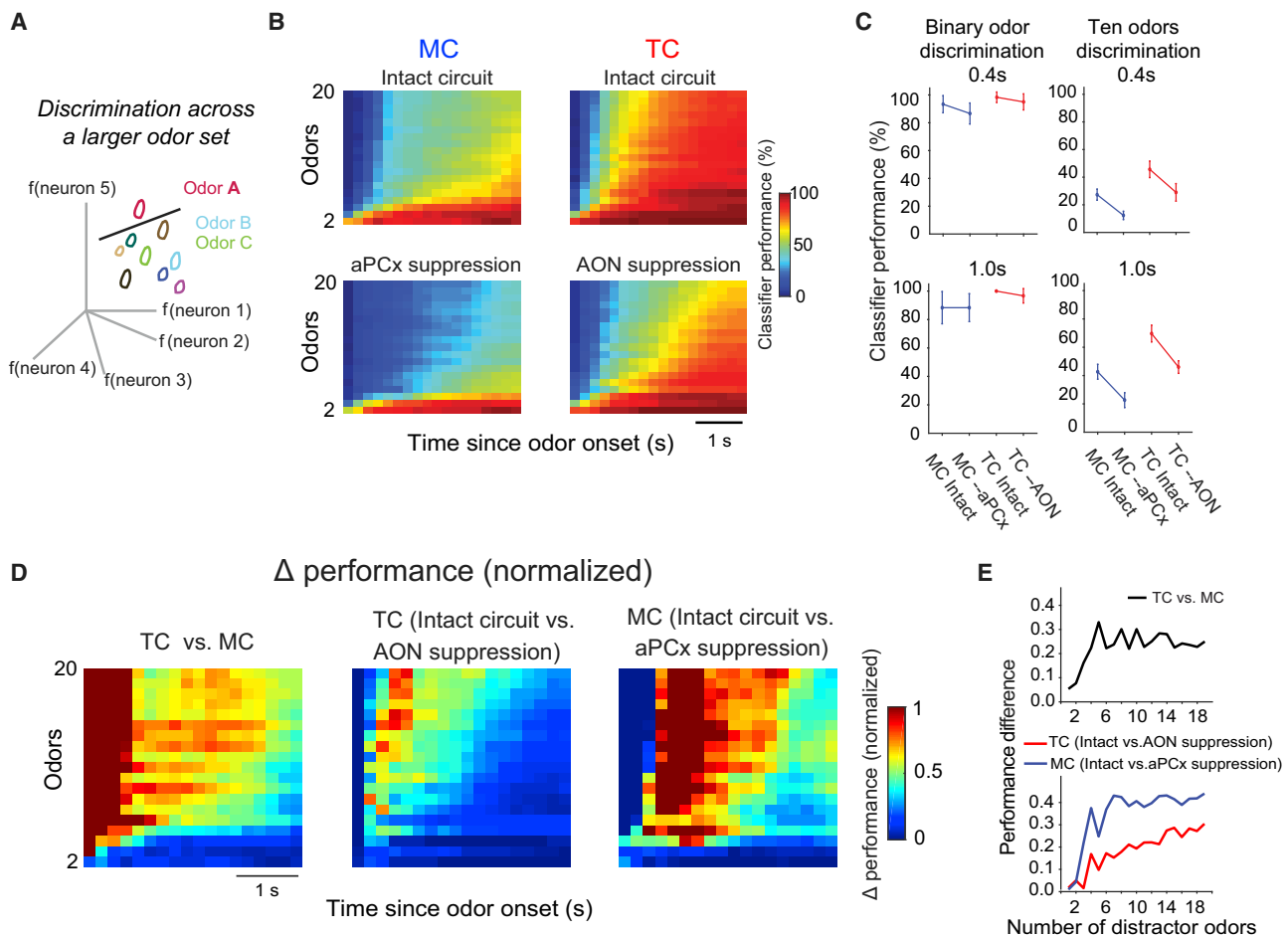
CellPress

Figure 7. TC ensembles-based decoders of odor identity across a larger odor panel outperform MC decoders that also depend more heavily on cortical feedback

(A) Cartoon schematics for discrimination across a larger (20) odor set. The decoder learns to group increasing number of odors (1–19) as distinct from the reference odor for a given classification, so as to discriminate any odor in the panel from any other. The number of odors included in the analysis is varied systematically from 2 to 20.

(B) 2D classification performance map (SVM, non-linear) for all four experimental conditions (MC: 5 FOVs, 4 mice, TC: 4 FOVs, 4 mice) in the discrimination across a larger (20) odor set decoding scheme. Abscissa represents the time axis (bin size = 200 ms), whereas the ordinate indicates varying the number of odors included using bootstrap re-sampling (ordinate, bin size = 1 odor).

(C) Classifier performance (Avg. ± 95% confidence interval) evaluated at two time points (0.4 and 1.0 s) for the MC (blue) and TC (red) decoders engaged in binary (left) and ten odor (right) discrimination.

(D) 2D performance difference index maps with increasing number of odor distractors (ordinate) and increasing time from odor onset (abscissa). (Left) TC- versus MC-based decoders; positive values indicate that performance is higher for TC than MC decoders. (Center) Change in performance of TCss decoders before versus after suppression of ipsi-AON feedback; (right) change in performance of MCs decoders before versus after suppression of aPCx feedback. Positive values indicate higher decoding performance in the intact circuit.

(E) Difference in classifier performance with increasing number of odor distractors. (Top) TCs versus MCs (black line) evaluated at 1.0 s since odor onset; (bottom) intact circuit versus preferred cortical target feedback suppression for MCs (blue) and TCs (red) separately. Baseline level performance of the decoder is 0. See also Figures S8 and S9 and Table S2.

contribution of cortical feedback from the piriform and AON to the decoding ability of MC and TC ensembles increased with the complexity of the task. Our results identify distinct functional feedforward-feedback loops supported by the MCs and TCs and their preferred cortical targets. As TCs innervate mainly brain regions other than the PCx, such as the AON and olfactory striatum (tubercle), these findings open venues for investigating the logic of the downstream neural circuits supporting decoding odor

identity beyond the canonical mitral-to-PCx pathway. Although activity from both the TCs-to-AON and MCs-to-PCx loops can be integrated to support the decoding of odor identity, these results indicate that the TCs-to-AON pathway plays a major role (Figure 8).

Our results are consistent with the proposed role of the AON in olfactory navigation, as comparator of differences in stimulus intensity across nostrils (Esquivelzeta Rabell et al., 2017; Kikuta
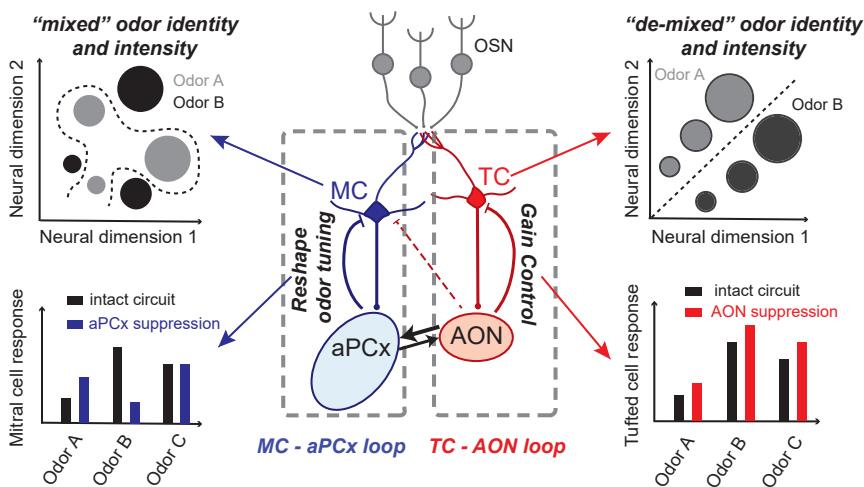
Figure 8. Summary cartoon of long-range functional loops involving the MCs and TCs and their major cortical targets
Cartoon schematics of functional specificity in two long-range loops that engage MCs and the aPCx (blue) and, respectively, TCs and the AON (red). Mixed (MC) and de-mixed (TC) representations of odor identity and intensity. TC ensemble-based decoders of odor identity and concentration outperform MC-based decoders which also depend more heavily on cortical feedback. Cortical bulbar feedback originating in the aPCx and AON regulates specifically the activity of its dominant bulb cell-type input and implements different computations. Piriform feedback specifically re-structures mitral responses, whereas feedback from AON preferentially controls the gain of tufted cell representations, without altering their odor tuning. OSNs, olfactory sensory neurons.

et al., 2010), and also further suggest that TC targets such as the AON and OT play key roles in representing odor identity (Haberly, 2001). Recent work indicates that activity in the tubercle reflects the association between odorants and reward outcome (Gadziola and Wesson, 2016; Gadziola et al., 2015; Millman and Murthy, 2020) and is re-organized in selective attention tasks (Carlson et al., 2018). The tubercle receives direct input from the bulb via both TC and MC axons (Haberly and Price, 1977; Nagayama et al., 2004; Skeen and Hall, 1977), as well as indirect input via the AON and PCx. Future investigation is necessary to determine the relative contribution of MC versus TC pathways in supporting these computations.

One potential limitation of the study is that we did not investigate the fast temporal patterning of spiking in specific sequences with respect to the respiration cycle, which may also contribute to identity decoding (Cury and Uchida, 2010; Dhawale et al., 2010; Gollisch and Meister, 2008; Hopfield, 1995; Li et al., 2015; Tank and Hopfield, 1987; Wilson et al., 2017). Although the temporal dynamics of calcium responses is slower compared with electrophysiology methods, technical constraints are unlikely to account for the differences reported in the performance of MC and TC ensembles (see STAR Methods). We cannot however rule out spike-timing-based decoding strategies where select group of neurons are responsible for representing the identity of specific stimuli. Thus, further investigation is required to elucidate the potential differences between TC and MC ensemble representations with spike-time resolution.

The specificity and functional segregation of cortical feedback action, preferentially targeting the dominant input cell type (Figures 3, 4, and 5), is surprising, given the wide potential for cross-talk either via reciprocal anatomical connections between the AON and PCx ipsilaterally (Hagiwara et al., 2012) or via dedicated TC- and MC-specific interneurons within the bulb (Geramita et al., 2016) that may receive convergent inputs from the AON and aPCx. Indeed, our observations that feedback originating in AON, although strongly regulating TC activity also modulates, albeit to a lesser degree, the responses of MCs ipsilaterally could be due to such cross-interactions. The differential effect on MC and TC responses, depending on the site of cortical inactivation, is consis-

tent with the presence of distinct granule cells that preferentially target each cell type (Geramita et al., 2016).

A feedforward-feedback loop architecture engaging multiple pathways enables both implementing different computations on inputs from the sensory periphery (e.g., bulb) via parallel streams, as well as cross-talk and comparisons across streams. Indeed, parallel functional streams have been identified in other sensory modalities (Dijkerman and de Haan, 2007; Goodale and Milner, 1992; Mishkin and Ungerleider, 1982; Rauschecker and Romanski, 2011; Schneider, 1969). The net effect of feedback from the AON is to proportionally suppress the feedforward input drive for each stimulus, thereby regulating the gain of tufted ensemble activity. This may prevent runaway excitation, without altering the specificity of responses (Figures 5 and 6). In contrast, the feedback from piriform specifically shapes the odor representations of MCs (modifies their odor tuning) and cannot be explained only by a simple gain control model (Figures 5 and S7). For both MC and TC decoding performance, cortical feedback became increasingly necessary for hard odor discriminations (Figures 6 and 7), in agreement with previous results (Lepousez et al., 2014; Li et al., 2018).

Given our findings, and consistent with previous work (Frank et al., 2019; Kay and Laurent, 1999; Lepousez et al., 2014; Li et al., 2018; Wilson and Sullivan, 2011), an interesting possibility is that the MCs-to-PCx loop is not primarily involved in the sensory aspects of odor identification, which appear well-supported by the TCs-to-AON pathway analyzed here. Recent work identified drift in the piriform odor responses which imposes constraints for robust representations of odor identity (Schoonover et al., 2021). Rather, the mitral-to-piriform loop may perform different computations ranging from specifically modifying odor representations during contextual learning and/or relaying sensory and sensorimotor predictions and errors in complex, fluctuating olfactory scenes. Within this framework, the tufted-to-AON pathway conveys odor identity and intensity information (Haberly, 2001) to the PCx that further uses it to engage these computations (Figure 8). Many studies employing either multiphoton imaging or electrophysiology established that the activity of MCs/TCs and the accuracy for

Neuron
Article

odorant identity decoding depends on the behavioral state. Decoding accuracy increases substantially as animals learn to differentiate odorants (Chu et al., 2016; Gschwend et al., 2015; Kudryavitskaya et al., 2021; Li et al., 2015; Losacco et al., 2020; Yamada et al., 2017). MC/TC odor representations are modulated as a function of prior experience (Kato et al., 2012; Vinograd et al., 2017), learning (Chu et al., 2016; Gschwend et al., 2015; Li et al., 2015; Losacco et al., 2020; Yamada et al., 2017), context (Koldaeva et al., 2019), and stimulus contingency (Kay and Laurent, 1999; Kudryavitskaya et al., 2021; Li et al., 2015). For example, while learning a binary discrimination task, MC ensembles became substantially more decorrelated compared with TCs, whereas both cell type responses were re-formatted (Yamada et al., 2017). In addition, following changes in odor-reward rules across different tasks, MC responses re-organized according to the odor value (Kudryavitskaya et al., 2021). Future investigation will elucidate the mechanisms by which the TCs-to-AON and MCs-to-PCx loops described here remain specific, the extent of their cross-talk and how they support relevant computations for guiding olfactory behaviors as a function of olfactory scene complexity, perceptual task, and stimulus contingency.

STAR★METHODS

Detailed methods are provided in the online version of this paper and include the following:

- KEY RESOURCES TABLE
- RESOURCE AVAILABILITY
  - Lead contact
  - Materials availability
  - Data and code availability
- EXPERIMENTAL MODEL AND SUBJECT DETAILS
- METHOD DETAILS
  - Surgery
  - Odor Stimulation
  - Multiphoton imaging
  - Pharmacology
  - Tracing of feedback fibers
  - Histology
  - Experimental design
- QUANTIFICATION AND STATISTICAL ANALYSIS
  - Pre-processing and detection of significant odor responses
  - Odor similarity (odor correlation)
  - Correlation between same odor responses across conditions
  - Dimensionality reduction (PCA and dPCA)
  - Decoding odor identity (sparse logistic regression and support vector machines)
  - Generalization to novel concentrations
  - Odor identification & concentration decoding
  - Concentration-invariant odor recognition
  - Discrimination across a larger (20) odor set
  - Quantifying the effect of cortical feedback suppression
  - Odor similarity-matching number of mitral cells and tufted cells

- Additional considerations for the decoding analyses
- Technical comments on response strength and its temporal dynamics
- Signal to noise ratio (SNR)
- Temporal dynamics of responses

AUTHOR CONTRIBUTIONS

Investigation, formal analyses, visualization, and writing – review and editing, H.C.; conceptualization, methodology, formal analysis, visualization, software, writing – original draft, and writing – review and editing, A.B.; data curation, visualization, validation, and writing – review and editing, M.D.; conceptualization, methodology, writing – original draft, writing – review and editing, supervision, project administration, and funding acquisition, D.F.A.

DECLARATION OF INTERESTS

The authors declare no competing interests.

REFERENCES

Abraham, N.M., Spors, H., Carleton, A., Margrie, T.W., Kuner, T., and Schaefer, A.T. (2004). Maintaining accuracy at the expense of speed: stimulus similarity defines odor discrimination time in mice. Neuron 44, 865–876. https://doi.org/10.1016/j.neuron.2004.11.017.

Andres, K.H. (1970). Anatomy and ultrastructure of the olfactory bulb in fish, amphibia, reptiles, birds, and mammals. In CIBA Foundation Symposium on Taste and Smell in Vertebrates (Churchill), pp. 177–194.

Aqrabawi, A.J., and Kim, J.C. (2018). Hippocampal projections to the anterior olfactory nucleus differentially convey spatiotemporal information during episodic odour memory. Nat. Commun. 9, 2735. https://doi.org/10.1038/s41467-018-05131-6.

Babadi, B., and Sompolinsky, H. (2014). Sparseness and expansion in sensory representations. Neuron 83, 1213–1226. https://doi.org/10.1016/j.neuron.2014.07.035.

Banerjee, A., Marbach, F., Anselmi, F., Koh, M.S., Davis, M.B., Garcia da Silva, P., Delevich, K., Oyibo, H.K., Gupta, P., Li, B., et al. (2015). An interglomerular circuit gates glomerular output and implements gain control in the mouse olfactory bulb. Neuron 87, 193–207. https://doi.org/10.1016/j.neuron.2015.06.019.

Bolding, K.A., and Franks, K.M. (2017). Complementary codes for odor identity and intensity in olfactory cortex. eLife 6, e22630.

Bolding, K.A., and Franks, K.M. (2018). Recurrent cortical circuits implement concentration-invariant odor coding. Science 361, eaat6904. https://doi.org/10.1126/science.aat6904.

Boyd, A.M., Kato, H.K., Komiyama, T., and Isaacson, J.S. (2015). Broadcasting of cortical activity to the olfactory bulb. Cell Rep 10, 1032–1039. https://doi.org/10.1016/j.celrep.2015.01.047.

Boyd, A.M., Sturgill, J.F., Poo, C., and Isaacson, J.S. (2012). Cortical feedback control of olfactory bulb circuits. Neuron 76, 1161–1174. https://doi.org/10.1016/j.neuron.2012.10.020.

Brunjes, P.C., Illig, K.R., and Meyer, E.A. (2005). A field guide to the anterior olfactory nucleus (cortex). Brain Res. Brain Res. Rev. 50, 305–335. https://doi.org/10.1016/j.brainresrev.2005.08.005.

Burton, S.D., and Urban, N.N. (2014). Greater excitability and firing irregularity of tufted cells underlies distinct afferent-evoked activity of olfactory bulb mitral and tufted cells. J. Physiol. 592, 2097–2118. https://doi.org/10.1113/jphysiol.2013.269886.

Carlson, K.S., Gadziola, M.A., Dauster, E.S., and Wesson, D.W. (2018). Selective attention controls olfactory decisions and the neural encoding of odors. Curr. Biol. 28, 2195–2205.e4. https://doi.org/10.1016/j.cub.2018.05.011.

Cavarretta, F., Burton, S.D., Igarashi, K.M., Shepherd, G.M., Hines, M.L., and Migliore, M. (2018). Parallel odor processing by mitral and middle tufted cells in the olfactory bulb. Sci. Rep. 8, 7625. https://doi.org/10.1038/s41598-018-25740-x.

Celani, A., Villermaux, E., and Vergassola, M. (2014). Odor landscapes in turbulent environments. Phys. Rev. X 4, 041015. https://doi.org/10.1103/PhysRevX.4.041015.

Chae, H., Kepple, D.R., Bast, W.G., Murthy, V.N., Koulakov, A.A., and Albeanu, D.F. (2019). Mosaic representations of odors in the input and output layers of the mouse olfactory bulb. Nat. Neurosci. 22, 1306–1317. https://doi.org/10.1038/s41593-019-0442-z.

Chen, T.-W., Wardill, T.J., Sun, Y., Pulver, S.R., Renninger, S.L., Baohan, A., Schreiter, E.R., Kerr, R.A., Orger, M.B., Jayaraman, V., et al. (2013). Ultrasensitive fluorescent proteins for imaging neuronal activity. Nature 499, 295–300. https://doi.org/10.1038/nature12354.

Choi, G.B., Stettler, D.D., Kallman, B.R., Bhaskar, S.T., Fleischmann, A., and Axel, R. (2011). Driving opposing behaviors with ensembles of piriform neurons. Cell 146, 1004–1015. https://doi.org/10.1016/j.cell.2011.07.041.

Chong, E., Moroni, M., Wilson, C., Shoham, S., Panzeri, S., and Rinberg, D. (2020). Manipulating synthetic optogenetic odors reveals the coding logic of olfactory perception. Science 368, eaba2357. https://doi.org/10.1126/science.aba2357.

Chu, M.W., Li, W.L., and Komiyama, T. (2016). Balancing the robustness and efficiency of odor representations during learning. Neuron 92, 174–186. https://doi.org/10.1016/j.neuron.2016.09.004.

Cury, K.M., and Uchida, N. (2010). Robust odor coding via inhalation-coupled transient activity in the mammalian olfactory bulb. Neuron 68, 570–585. https://doi.org/10.1016/j.neuron.2010.09.040.

Dhawale, A.K., Hagiwara, A., Bhalla, U.S., Murthy, V.N., and Albeanu, D.F. (2010). Non-redundant odor coding by sister mitral cells revealed by light addressable glomeruli in the mouse. Nat. Neurosci. 13, 1404–1412. https://doi.org/10.1038/nn.2673.

DiCarlo, J.J., Zoccolan, D., and Rust, N.C. (2012). How does the brain solve visual object recognition? Neuron 73, 415–434. https://doi.org/10.1016/j.neuron.2012.01.010.

Dijkerman, H.C., and de Haan, E.H.F. (2007). Somatosensory processes subserving perception and action. Behav. Brain Sci. 30, 189–201. discussion 201–239. https://doi.org/10.1017/S0140525X07001392.

Esquivelzeta Rabell, J., Mutlu, K., Noutel, J., Martin del Olmo, P., and Haesler, S. (2017). Spontaneous rapid odor source localization behavior requires interhemispheric communication. Curr. Biol. 27, 1542–1548.e4. https://doi.org/10.1016/j.cub.2017.04.027.

Fantana, A.L., Soucy, E.R., and Meister, M. (2008). Rat olfactory bulb mitral cells receive sparse glomerular inputs. Neuron 59, 802–814. https://doi.org/10.1016/j.neuron.2008.07.039.

Frank, T., Mönig, N.R., Satou, C., Higashijima, S.I., and Friedrich, R.W. (2019). Associative conditioning remaps odor representations and modifies inhibition in a higher olfactory brain area. Nat. Neurosci. 22, 1844–1856. https://doi.org/10.1038/s41593-019-0495-z.

Fukunaga, I., Berning, M., Kollo, M., Schmaltz, A., and Schaefer, A.T. (2012). Two distinct channels of olfactory bulb output. Neuron 75, 320–329. https://doi.org/10.1016/j.neuron.2012.05.017.

Gadziola, M.A., Tylicki, K.A., Christian, D.L., and Wesson, D.W. (2015). The olfactory tubercle encodes odor valence in behaving mice. J. Neurosci. 35, 4515–4527. https://doi.org/10.1523/JNEUROSCI.4750-14.2015.

Gadziola, M.A., and Wesson, D.W. (2016). The neural representation of goal-directed actions and outcomes in the ventral striatum's olfactory tubercle. J. Neurosci. 36, 548–560. https://doi.org/10.1523/JNEUROSCI.3328-15.2016.

Geramita, M., and Urban, N.N. (2017). Differences in glomerular-layer-mediated feedforward inhibition onto mitral and tufted cells lead to distinct modes of intensity coding. J. Neurosci. 37, 1428–1438. https://doi.org/10.1523/JNEUROSCI.2245-16.2016.

Geramita, M.A., Burton, S.D., and Urban, N.N. (2016). Distinct lateral inhibitory circuits drive parallel processing of sensory information in the mammalian olfactory bulb. eLife 5, e16039. https://doi.org/10.7554/eLife.16039.

Ghosh, S., Larson, S.D., Hefzi, H., Marnoy, Z., Cutforth, T., Dokka, K., and Baldwin, K.K. (2011). Sensory maps in the olfactory cortex defined by long-range viral tracing of single neurons. Nature 472, 217–220. https://doi.org/10.1038/nature09945.

Gire, D.H., Franks, K.M., Zak, J.D., Tanaka, K.F., Whitesell, J.D., Mulligan, A.A., Hen, R., and Schoppa, N.E. (2012). Mitral cells in the olfactory bulb are mainly excited through a multistep signaling path. J. Neurosci. 32, 2964–2975. https://doi.org/10.1523/JNEUROSCI.5580-11.2012.

Gollisch, T., and Meister, M. (2008). Rapid neural coding in the retina with relative spike latencies. Science 319, 1108–1111. https://doi.org/10.1126/science.1149639.

Goodale, M.A., and Milner, A.D. (1992). Separate visual pathways for perception and action. Trends Neurosci 15, 20–25. https://doi.org/10.1016/0166-2236(92)90344-8.

Gottfried, J.A. (2010). Central mechanisms of odour object perception. Nat. Rev. Neurosci. 11, 628–641. https://doi.org/10.1038/nrn2883.

Grabska-Barwińska, A., Barthelmé, S., Beck, J., Mainen, Z.F., Pouget, A., and Latham, P.E. (2017). A probabilistic approach to demixing odors. Nat. Neurosci. 20, 98–106. https://doi.org/10.1038/nn.4444.

Gschwend, O., Abraham, N.M., Lagier, S., Begnaud, F., Rodriguez, I., and Carleton, A. (2015). Neuronal pattern separation in the olfactory bulb improves odor discrimination learning. Nat. Neurosci. 18, 1474–1482. https://doi.org/10.1038/nn.4089.

Gupta, P., Albeanu, D.F., and Bhalla, U.S. (2015). Olfactory bulb coding of odors, mixtures and sniffs is a linear sum of odor time profiles. Nat. Neurosci. 18, 272–281. https://doi.org/10.1038/nn.3913.

Haberly, L.B. (2001). Parallel-distributed processing in olfactory cortex: new insights from morphological and physiological analysis of neuronal circuitry. Chem. Senses 26, 551–576.

Haberly, L.B., and Price, J.L. (1977). The axonal projection patterns of the mitral and tufted cells of the olfactory bulb in the rat. Brain Res 129, 152–157. https://doi.org/10.1016/0006-8993(77)90978-7.

Hagiwara, A., Pal, S.K., Sato, T.F., Wienisch, M., and Murthy, V.N. (2012). Optophysiological analysis of associational circuits in the olfactory cortex. Front. Neural Circuits 6, 18. https://doi.org/10.3389/fncir.2012.00018.

Hong, H., Yamins, D.L.K., Majaj, N.J., and DiCarlo, J.J. (2016). Explicit information for category-orthogonal object properties increases along the ventral stream. Nat. Neurosci. 19, 613–622. https://doi.org/10.1038/nn.4247.

Hopfield, J.J. (1995). Pattern recognition computation using action potential timing for stimulus representation. Nature 376, 33–36. https://doi.org/10.1038/376033a0.

Igarashi, K.M., Ieki, N., An, M., Yamaguchi, Y., Nagayama, S., Kobayakawa, K., Kobayakawa, R., Tanifuji, M., Sakano, H., Chen, W.R., et al. (2012). Parallel mitral and tufted cell pathways route distinct odor information to different targets in the olfactory cortex. J. Neurosci. 32, 7970–7985. https://doi.org/10.1523/JNEUROSCI.0154-12.2012.

Jordan, R., Fukunaga, I., Kollo, M., and Schaefer, A.T. (2018). Active sampling state dynamically enhances olfactory bulb odor representation. Neuron 98, 1214–1228.e5. https://doi.org/10.1016/j.neuron.2018.05.016.

Kapoor, V., Provost, A.C., Agarwal, P., and Murthy, V.N. (2016). Activation of raphe nuclei triggers rapid and distinct effects on parallel olfactory bulb output channels. Nat. Neurosci. 19, 271–282. https://doi.org/10.1038/nn.4219.

Kato, H.K., Chu, M.W., Isaacson, J.S., and Komiyama, T. (2012). Dynamic sensory representations in the olfactory bulb: modulation by wakefulness and experience. Neuron 76, 962–975. https://doi.org/10.1016/j.neuron.2012.09.037.

Kay, L.M., and Laurent, G. (1999). Odor- and context-dependent modulation of mitral cell activity in behaving rats. Nat. Neurosci. 2, 1003–1009. https://doi.org/10.1038/14801.

Kerlin, A.M., Andermann, M.L., Berezovskii, V.K., and Reid, R.C. (2010). Broadly tuned response properties of diverse inhibitory neuron subtypes in mouse visual cortex. Neuron 67, 858–871. https://doi.org/10.1016/j.neuron.2010.08.002.

Khan, A.G., Poort, J., Chadwick, A., Blot, A., Sahani, M., Mrsic-Flogel, T.D., and Hofer, S.B. (2018). Distinct learning-induced changes in stimulus selectivity and interactions of GABAergic interneuron classes in visual cortex. Nat. Neurosci. 21, 851–859. https://doi.org/10.1038/s41593-018-0143-z.

Kikuta, S., Fletcher, M.L., Homma, R., Yamasoba, T., and Nagayama, S. (2013). Odorant response properties of individual neurons in an olfactory glomerular module. Neuron 77, 1122–1135. https://doi.org/10.1016/j.neuron.2013.01.022.

Kikuta, S., Sato, K., Kashiwadani, H., Tsunoda, K., Yamasoba, T., and Mori, K. (2010). From the Cover: Neurons in the anterior olfactory nucleus pars externa detect right or left localization of odor sources. Proc. Natl. Acad. Sci. USA 107, 12363–12368. https://doi.org/10.1073/pnas.1003999107.

Kobak, D., Brendel, W., Constantinidis, C., Feierstein, C.E., Kepecs, A., Mainen, Z.F., Qi, X.-L., Romo, R., Uchida, N., and Machens, C.K. (2016). Demixed principal component analysis of neural population data. eLife 5, e10989. https://doi.org/10.7554/eLife.10989.

Koldaeva, A., Schaefer, A.T., and Fukunaga, I. (2019). Rapid task-dependent tuning of the mouse olfactory bulb. eLife 8, e43558. https://doi.org/10.7554/eLife.43558.

Koulakov, A.A., and Rinberg, D. (2011). Sparse incomplete representations: a potential role of olfactory granule cells. Neuron 72, 124–136. https://doi.org/10.1016/j.neuron.2011.07.031.

Kudryavitskaya, E., Marom, E., Shani-Narkiss, H., Pash, D., and Mizrahi, A. (2021). Flexible categorization in the mouse olfactory bulb. Curr. Biol. 31, 1616–1631.e4. https://doi.org/10.1016/j.cub.2021.01.063.

Lepousez, G., Nissant, A., Bryant, A.K., Gheusi, G., Greer, C.A., and Lledo, P.-M. (2014). Olfactory learning promotes input-specific synaptic plasticity in adult-born neurons. Proc. Natl. Acad. Sci. USA 111, 13984–13989. https://doi.org/10.1073/pnas.1404991111.

Li, A., Gire, D.H., and Restrepo, D. (2015). ϒ spike-field coherence in a population of olfactory bulb neurons differentiates between odors irrespective of associated outcome. J. Neurosci. 35, 5808–5822. https://doi.org/10.1523/JNEUROSCI.4003-14.2015.

Li, W.L., Chu, M.W., Wu, A., Suzuki, Y., Imayoshi, I., and Komiyama, T. (2018). Adult-born neurons facilitate olfactory bulb pattern separation during task engagement. eLife 7, e33006. https://doi.org/10.7554/eLife.33006.

Losacco, J., Ramirez-Gordillo, D., Gilmer, J., and Restrepo, D. (2020). Learning improves decoding of odor identity with phase-referenced oscillations in the olfactory bulb. eLife 9, e52583. https://doi.org/10.7554/eLife.52583.

Markopoulos, F., Rokni, D., Gire, D.H., and Murthy, V.N. (2012). Functional properties of cortical feedback projections to the olfactory bulb. Neuron 76, 1175–1188. https://doi.org/10.1016/j.neuron.2012.10.028.

Mathis, A., Rokni, D., Kapoor, V., Bethge, M., and Murthy, V.N. (2016). Reading out olfactory receptors: feedforward circuits detect odors in mixtures without demixing. Neuron 91, 1110–1123. https://doi.org/10.1016/j.neuron.2016.08.007.

Matsutani, S. (2010). Trajectory and terminal distribution of single centrifugal axons from olfactory cortical areas in the rat olfactory bulb. Neuroscience 169, 436–448. https://doi.org/10.1016/j.neuroscience.2010.05.001.

Meredith, M. (1986). Patterned response to odor in mammalian olfactory bulb: the influence of intensity. J. Neurophysiol. 56, 572–597.

Millman, D.J., and Murthy, V.N. (2020). Rapid learning of odor–value association in the olfactory striatum. J. Neurosci. 40, 4335–4347. https://doi.org/10.1523/JNEUROSCI.2604-19.2020.

Miri, A., Warriner, C.L., Seely, J.S., Elsayed, G.F., Cunningham, J.P., Churchland, M.M., and Jessell, T.M. (2017). Behaviorally selective engagement of short-latency effector pathways by motor cortex. Neuron 95, 683–696.e11. https://doi.org/10.1016/j.neuron.2017.06.042.

Mishkin, M., and Ungerleider, L.G. (1982). Contribution of striate inputs to the visuospatial functions of parieto-preoccipital cortex in monkeys. Behav. Brain Res. 6, 57–77. https://doi.org/10.1016/0166-4328(82)90081-x.

Miura, K., Mainen, Z.F., and Uchida, N. (2012). Odor representations in olfactory cortex: distributed rate coding and decorrelated population activity. Neuron 74, 1087–1098. https://doi.org/10.1016/j.neuron.2012.04.021.

Mori, K., Kishi, K., and Ojima, H. (1983). Distribution of dendrites of mitral, displaced mitral, tufted, and granule cells in the rabbit olfactory bulb. J. Comp. Neurol. 219, 339–355. https://doi.org/10.1002/cne.902190308.

Moskowitz, H.R., Dravnieks, A., and Klarman, L.A. (1976). Odor intensity and pleasantness for a diverse set of odorants. Percept. Psychophys. 19, 122–128. https://doi.org/10.3758/BF03204218.

Nagayama, S., Enerva, A., Fletcher, M.L., Masurkar, A.V., Igarashi, K.M., Mori, K., and Chen, W.R. (2010). Differential axonal projection of mitral and tufted cells in the mouse main olfactory system. Front. Neural Circuits 4, 120. https://doi.org/10.3389/fncir.2010.00120.

Nagayama, S., Takahashi, Y.K., Yoshihara, Y., and Mori, K. (2004). Mitral and tufted cells differ in the decoding manner of odor maps in the rat olfactory bulb. J. Neurophysiol. 91, 2532–2540. https://doi.org/10.1152/jn.01266.2003.

Oettl, L.-L., Ravi, N., Schneider, M., Scheller, M.F., Schneider, P., Mitre, M., da Silva Gouveia, M., Froemke, R.C., Chao, M.V., Young, W.S., et al. (2016). Oxytocin enhances social recognition by modulating cortical control of early olfactory processing. Neuron 90, 609–621. https://doi.org/10.1016/j.neuron.2016.03.033.

Okobi, D.E., Banerjee, A., Matheson, A.M.M., Phelps, S.M., and Long, M.A. (2019). Motor cortical control of vocal interaction in Neotropical singing mice. Science 363, 983–988. https://doi.org/10.1126/science.aau9480.

Oswald, A.-M., and Urban, N.N. (2012). There and back again: the corticobulbar loop. Neuron 76, 1045–1047. https://doi.org/10.1016/j.neuron.2012.12.006.

Otazu, G.H., Chae, H., Davis, M.B., and Albeanu, D.F. (2015). Cortical feedback decorrelates olfactory bulb output in awake mice. Neuron 86, 1461–1477. https://doi.org/10.1016/j.neuron.2015.05.023.

Pashkovski, S.L., Iurilli, G., Brann, D., Chicharro, D., Drummey, K., Franks, K.M., Panzeri, S., and Datta, S.R. (2020). Structure and flexibility in cortical representations of odour space. Nature 583, 253–258. https://doi.org/10.1038/s41586-020-2451-1.

Peron, S.P., Freeman, J., Iyer, V., Guo, C., and Svoboda, K. (2015). A cellular resolution map of barrel cortex activity during tactile behavior. Neuron 86, 783–799. https://doi.org/10.1016/j.neuron.2015.03.027.

Poo, C., and Isaacson, J.S. (2011). A major role for intracortical circuits in the strength and tuning of odor-evoked excitation in olfactory cortex. Neuron 72, 41–48. https://doi.org/10.1016/j.neuron.2011.08.015.

Rauschecker, J.P., and Romanski, L.M. (2011). Auditory cortical organization: evidence for functional streams. In The Auditory Cortex, J.A. Winer and C.E. Schreiner, eds. (Springer), pp. 99–116.

Rennaker, R.L., Chen, C.-F.F., Ruyle, A.M., Sloan, A.M., and Wilson, D.A. (2007). Spatial and temporal distribution of odorant-evoked activity in the piriform cortex. J. Neurosci. 27, 1534–1542. https://doi.org/10.1523/JNEUROSCI.4072-06.2007.

Rokni, D., Hemmelder, V., Kapoor, V., and Murthy, V.N. (2014). An olfactory cocktail party: figure-ground segregation of odorants in rodents. Nat. Neurosci. 17, 1225–1232. https://doi.org/10.1038/nn.3775.

Roland, B., Deneux, T., Franks, K.M., Bathellier, B., and Fleischmann, A. (2017). Odor identity coding by distributed ensembles of neurons in the mouse olfactory cortex. eLife 6, e26337. https://doi.org/10.7554/eLife.26337.

Rothermel, M., and Wachowiak, M. (2014). Functional imaging of cortical feedback projections to the olfactory bulb. Front. Neural Circuits 8, 73. https://doi.org/10.3389/fncir.2014.00073.

Rust, N.C., and DiCarlo, J.J. (2010). Selectivity and tolerance ("invariance") both increase as visual information propagates from cortical area V4 to. J. Neurosci. 30, 12978–12995. https://doi.org/10.1523/JNEUROSCI.0179-10.2010.

Schaffer, E.S., Stettler, D.D., Kato, D., Choi, G.B., Axel, R., and Abbott, L.F. (2018). Odor perception on the two sides of the brain: consistency Despite randomness. Neuron 98, 736–742.e3. https://doi.org/10.1016/j.neuron.2018.04.004.

Schneider, G.E. (1969). Two visual systems. Science 163, 895–902. https://doi.org/10.1126/science.163.3870.895.

Schoonover, C.E., Ohashi, S.N., Axel, R., and Fink, A.J.P. (2021). Representational drift in primary olfactory cortex. Nature 594, 541–546. https://doi.org/10.1038/s41586-021-03628-7.

Schwarz, D., Kollo, M., Bosch, C., Feinauer, C., Whiteley, I., Margrie, T.W., Cutforth, T., and Schaefer, A.T. (2018). Architecture of a mammalian glomerular domain revealed by novel volume electroporation using nanoengineered microelectrodes. Nat. Commun. 9, 183. https://doi.org/10.1038/s41467-017-02560-7.

Shepherd, G.M. (1972). Synaptic organization of the mammalian olfactory bulb. Physiol. Rev. 52, 864–917.

Shepherd, G.M. (2003). The Synaptic Organization of the Brain (Oxford University Press).

Shipley, M.T., and Adamek, G.D. (1984). The connections of the mouse olfactory bulb: a study using orthograde and retrograde transport of wheat germ agglutinin conjugated to horseradish peroxidase. Brain Res. Bull. 12, 669–688.

Sirotin, Y.B., Shusterman, R., and Rinberg, D. (2015). Neural coding of perceived odor intensity. eNeuro 2. https://doi.org/10.1523/ENEURO.0083-15.2015.

Skeen, L.C., and Hall, W.C. (1977). Efferent projections of the main and the accessory olfactory bulb in the tree shrew (Tupaia glis). J. Comp. Neurol. 172, 1–35. https://doi.org/10.1002/cne.901720102.

Sosulski, D.L., Bloom, M.L., Cutforth, T., Axel, R., and Datta, S.R. (2011). Distinct representations of olfactory information in different cortical centres. Nature 472, 213–216. https://doi.org/10.1038/nature09868.

Stettler, D.D., and Axel, R. (2009). Representations of odor in the piriform cortex. Neuron 63, 854–864. https://doi.org/10.1016/j.neuron.2009.09.005.

Tank, D.W., and Hopfield, J.J. (1987). Neural computation by concentrating information in time. Proc. Natl. Acad. Sci. USA 84, 1896–1900.

Tantirigama, M.L.S., Huang, H.H.-Y., and Bekkers, J.M. (2017). Spontaneous activity in the piriform cortex extends the dynamic range of cortical odor coding. Proc. Natl. Acad. Sci. USA 114, 2407–2412. https://doi.org/10.1073/pnas.1620939114.

Tian, L., Hires, S.A., Mao, T., Huber, D., Chiappe, M.E., Chalasani, S.H., Petreanu, L., Akerboom, J., McKinney, S.A., Schreiter, E.R., et al. (2009). Imaging neural activity in worms, flies and mice with improved GCaMP calcium indicators. Nat. Meth. 6, 875–881. https://doi.org/10.1038/nmeth.1398.

Uchida, N., Kepecs, A., and Mainen, Z.F. (2006). Seeing at a glance, smelling in a whiff: rapid forms of perceptual decision making. Nat. Rev. Neurosci. 7, 485–491. https://doi.org/10.1038/nrn1933.

Uchida, N., and Mainen, Z.F. (2003). Speed and accuracy of olfactory discrimination in the rat. Nat. Neurosci. 6, 1224–1229. https://doi.org/10.1038/nn1142.

Vinograd, A., Livneh, Y., and Mizrahi, A. (2017). History-dependent odor processing in the mouse olfactory bulb. J. Neurosci. 37, 12018–12030. https://doi.org/10.1523/JNEUROSCI.0755-17.2017.

Wang, C.Y., Liu, Z., Ng, Y.H., and Südhof, T.C. (2020). A synaptic circuit required for acquisition but not recall of social transmission of food preference. Neuron 107, 144–157.e4. https://doi.org/10.1016/j.neuron.2020.04.004.

Wilson, C.D., Serrano, G.O., Koulakov, A.A., and Rinberg, D. (2017). A primacy code for odor identity. Nat. Commun. 8, 1477. https://doi.org/10.1038/s41467-017-01432-4.

Wilson, D.A., and Sullivan, R.M. (2011). Cortical processing of odor objects. Neuron 72, 506–519. https://doi.org/10.1016/j.neuron.2011.10.027.

Yamada, Y., Bhaukaurally, K., Madarász, T.J., Pouget, A., Rodriguez, I., and Carleton, A. (2017). Context- and output layer-dependent long-term ensemble plasticity in a sensory circuit. Neuron 93, 1198–1212.e5. https://doi.org/10.1016/j.neuron.2017.02.006.

Zariwala, H.A., Kepecs, A., Uchida, N., Hirokawa, J., and Mainen, Z.F. (2013). The limits of deliberation in a perceptual decision task. Neuron 78, 339–351. https://doi.org/10.1016/j.neuron.2013.02.010.

🔗 **CellPress**

STAR★METHODS

KEY RESOURCES TABLE

REAGENT or RESOURCE	SOURCE	IDENTIFIER
Experimental models: Organism strains		
AI95 mice: B6J.Cg-*Gt(ROSA)26Sortm95.1 (CAG-GCaMP6f)Hze*/MwarJ	Jackson laboratory	RRID: IMSR_JAX:028865
AI38 mice: B6;129S-*Gt(ROSA)26Sortm38 (CAG-GCaMP3)Hze*/J	Jackson laboratory	RRID: IMSR_JAX:014538
Tbet-Cre mice: B6;CBA-Tg(Tbx21-cre)1Dlc/J	Jackson laboratory	RRID: IMSR_JAX:024507
vGlut1-Cre mice: B6;129S-*Slc17a7tm1.1(cre)Hze*/J	Jackson Laboratory	RRID: IMSR_JAX:023527
Bacterial and virus strains		
AAV2/9-CAG-FLEX-GFP	UNC vector core	N/A
Chemicals, peptides, and recombinant proteins		
Muscimol hydrobromide (MW=195.01)	Sigma Aldrich	N/A
Deposited data		
Normalized fluorescence signal of individual ROIs	This paper, Mendeley Data and Github	https://github.com/TeamAlbeanu/LongRangeFunctionalLoops.git
Software and algorithms		
ImageJ (Fiji)		https://fiji.sc/
MATLAB	Mathworks	RRID: SCR_001622; https://www.mathworks.com/products/matlab.html
Data processing and analysis scripts	This paper, Mendeley Data and Github	https://zenodo.org/badge/latestdoi/524097950

RESOURCE AVAILABILITY

Lead contact
Further information and requests for resources and reagents should be directed to and will be fulfilled by the lead contact, Dinu F. Albeanu (albeanu@cshl.edu).

Materials availability
This study did not generate new, unique reagents.

Data and code availability
All data matrices representing mitral and tufted cell odor responses included in the analyses presented here are available upon request and are also provided in a Mendeley data repository: https://data.mendeley.com/datasets/d4w9j6tcvb/draft?a=916c252f-3936-4cc8-98d8-ab0b8db85cfa.

The code used for analysis is available on github: https://github.com/TeamAlbeanu/LongRangeFunctionalLoops.git

DOI: https://zenodo.org/badge/latestdoi/524097950.

Any additional information required to reanalyze the data reported in this work paper is available from the lead contact upon request.

EXPERIMENTAL MODEL AND SUBJECT DETAILS

For our experiments, we used adult (>12 weeks old, 25-30g) mice (males and females) of the following strains: B6J.Cg-*Gt(ROSA) 26Sortm95.1(CAG-GCaMP6f)Hze*/MwarJ (AI95); B6;129S-*Gt(ROSA)26Sortm38(CAG-GCaMP3)Hze*/J (AI38), *B6;CBA-Tg(Tbx21-cre)1Dlc/J* (TBET-Cre) and B6;129S-*Slc17a7tm1.1(cre)Hze*/J (vGlut1-Cre). All animal procedures conformed to NIH guidelines and were approved by the Animal Care and Use Committee of Cold Spring Harbor Laboratory.

METHOD DETAILS

Surgery

38 adult Tbet-Cre X AI95 or AI38 mice (males and females > 12 weeks old, 25 – 30 g) were administered meloxicam (5mg/kg) and dexamethasone (1mg/kg) 2 hours before surgery. Mice were anesthetized with ketamine/xylazine (initial dose 70/7mg per kg), and supplemented every 45 minutes. Lack of pain reflexes was monitored throughout the procedure. Mice were positioned such that the skull dorsal surface is horizontal, and implanted stereotaxically with cannulae (26 Gauge, Plastics One) bilaterally in the piriform cortex (inserted at 50 degrees from the normal to the brain surface, -4.0 mm (A-P) and 2.4 mm (M-L) from bregma, 7.5 mm deep from surface, corresponding to +1.7 mm A-P, 2.4 mm M-L, 4.0 mm depth from surface at 0 degrees from the normal), and respectively unilaterally in the AON (at 56 degree from the normal, -4.0 mm (A-P) and 1.0 mm (M-L) from bregma, 7.5 mm deep from surface, corresponding to +2.25 mm A-P, 1.0 mm M-L, 4.0 mm depth from surface at 0 degrees from the normal, AON posterior part - AOP). At the same time, a chronic window was implanted above the dorsal aspect of the olfactory bulbs, and a titanium headbar was attached to the skull as previously described (Otazu et al., 2015) to fixate the animal during the imaging sessions. Meloxicam (5mg/kg) was administered for 5 – 7 days following surgery. Mice were allowed to recover for at least 10 days and further habituated before multi-photon imaging.

Odor Stimulation

Custom-built odors delivery machines were used to present odors automatically under computer control of solenoid valves (Chae et al., 2019; Otazu et al., 2015). Two sets of odors were used: Odor Set A comprising of 5 odors across 4 concentrations, spanning $1:10^4$ to $1:10^1$ nominal oil dilutions, and Odor Set B, comprising of 20 odors, sampled at 1:100 mineral oil dilution, Table S1. Odors (1 l/min) were presented in 4s pulses every 1 minute preceded by the acquisition of 10-12s of air baseline and followed by 7-10s of air recovery periods. To minimize odor contamination across trials, during the inter-trial interval, a high flow air stream (>10 l/min) was pushed through teflon coated tubing conduits of the odor delivery machines to an exhaust vent, while the animal's snout was exposed to fresh air matched at 1 l/min flow rate. Each stimulus was typically repeated 3-5 times before, as well as after-muscimol or saline injections. The concentration of the odors delivered to the mouse for concentration experiments was characterized using a photo-ionization device (PID; Aurora Scientific) and spanned a range between ~0.02% and 10% saturated vapor pressure (Banerjee et al., 2015; Otazu et al., 2015). The same PID was used to determine the time course of the odor waveform and the reliability of odor stimulation. On average, across odors and concentration range sampled, stimuli took 315 +/- 119ms to reach 80% of peak PID value (rising time, Figure S1A). This delay in stimulus delivery was accounted for in the decoding analyses (Figures 2, 6, 7, S2, S8, and S9) by removing the corresponding frames from the analysis. For both mitral and tufted cells, responses to Odor Set A were monitored using multiphoton imaging of GCaMP6f signals and to Odor Set B of GCaMP3 signals respectively. For each odor set and activity indicators considered, matched numbers of responsive mitral and tufted cells were included in the analysis.

Multiphoton imaging

We used a custom-built multiphoton microscope coupled with Chameleon Ultra II Ti:Sapphire femtosecond pulsed laser (Coherent). The scanning system projected the incident laser beam tuned at 930nm through a scan lens and tube lens to backfill the aperture of an Olympus 20X, 1.0 NA objective. The shortest possible optical path was used to bring the laser onto a galvanometric mirrors scanning (6215HB, Cambridge Technologies) or resonant scanning head (12 KHz, High Stability 8315K - CRS-12 Set, Cambridge Technologies). Signals were acquired using a GaAsP PMT (H10770PB-40, Hamamatsu), amplified, filtered (DHPCA-100, Femto) and digitized at 200 MHz (NI PXIe-7966R FPGA Module, NI5772 Digitizer Adapter Module). Acquisition and scanning (10 Hz: Odor Set B or 50Hz: Odor Set A) were performed using custom-written software in Labview (National Instruments) including Iris (Keller Lab, FMI). During a typical imaging session, animals were head-fixed under the two photon microscope and habituated to odors and the sound of the scanning galvos (45 min). Laser power was adjusted to minimize bleaching (<40 mW). Tufted cells were identified based on the location of their somata in the external plexiform layer (125-175 μm from the surface), while mitral cells were identified as a densely packed monolayer of larger somata located 225-275 μm deep from bulb surface. Spread across the external plexiform layer, several subclasses of tufted cells have been described (superficial, middle, internal) at varying depths from bulb surface (Mori et al., 1983; Schwarz et al., 2018). Here, we probed primarily the activity of middle tufted cells, and further investigation is needed to determine whether different tufted cell subsets relay distinct odor representations.

Pharmacology

Cannulae were implanted bilaterally for aPCx and unilaterally for AON suppression experiments (Figure S3). Piriform cortex feedback to the OB originates mainly in the anterior apart of the piriform cortex, hence we focused our muscimol suppression experiments on aPCx (Boyd et al., 2012; Markopoulos et al., 2012; Oswald and Urban, 2012; Otazu et al., 2015). For a given imaging session, muscimol/saline was injected in only one hemisphere. After imaging a given field of view (baseline), muscimol (muscimol hydrobromide, MW=195.01, Sigma) dissolved in cortex buffer was used to suppress neuronal activity in the aPCx or AON (0.5mg/ml, 1μl injected into aPCx over 5 min, 0.7 μl injected into AON over 3.5 min). To avoid the spread of muscimol into the olfactory bulb, and accounting for its smaller size, we injected less volume into the AON (0.7 μl) than aPCx (1 μl). Care was taken to identify the same cell bodies in the field of view before and after the injection of muscimol or saline, waiting 20-30 minutes post-injection before re-starting the imaging

session. No apparent changes in animals' sniffing, whisking or motor behaviors were observed upon muscimol injection. In a previous study (Otazu et al., 2015), we have quantified the spread of muscimol into aPCx, calibrating it using comparatively larger volumes of fluorescent muscimol bodipy (Life Science Technologies) to account for the difference in their molecular weights. In this study, we used the same muscimol injection protocol, and identified the injection site (for either muscimol or saline) once the imaging session was completed, by injecting fluorescent muscimol as previously described (Otazu et al., 2015). Note that any spread of muscimol from AON to aPCx or vice versa would only result in decreasing the specificity observed in the AON or aPCx feedback action on the mitral versus tufted cells. Brains were perfused in PFA, and 100-200μm sagittal slices were cut and imaged under an epifluorescence microscope. For control experiments (saline), only cortex buffer was used.

Since AON is a functionally heterogeneous structure comprised of several nuclei (Brunjes et al., 2005; Shepherd, 2003) which may multiplex information ranging from odor localization and identification to episodic memory (Aqrabawi and Kim, 2018) and social cues (Oettl et al., 2016; Wang et al., 2020), further studies are necessary to investigate any differences in feedforward-feedback action across different AON nuclei and tufted cell ensembles.

We have performed experiments lasting up to two hours after muscimol injection. For the whole duration of the experiment, we observed an increased in the response amplitude, number of responses per cell and pairwise odor correlation, as compared to saline controls, suggesting that the effect of the muscimol was still present throughout the imaging session. This is consistent with other studies using comparable dosage of muscimol, where the effect has been shown to last at least 2 hours (Miri et al., 2017; Okobi et al., 2019). Note that if the effect of the muscimol diminished gradually during the experiment, this would impose a lower bound interpretation on the effects that we report upon cortical suppression. We also observed an increase in the baseline fluorescence post-muscimol, but could not quantify it directly given the parallel tendency of decrease in signal across time during the imaging session. In addition, post-muscimol injection, the fraction of suppressed responses was lower than before muscimol.

Previous reports showed that the duration of responses in the olfactory cortex is shaped by several factors including the duration and strength of odor stimulation and the brain state (Poo and Isaacson, 2011; Rennaker et al., 2007; Roland et al., 2017; Schoonover et al., 2021; Stettler and Axel, 2009; Tantirigama et al., 2017). Here we suppressed the cortical feedback over many hours by injecting muscimol in the aPCx or AON. Future investigation is required to evaluate the role of transient of cortical inactivation as a function of odor statistics.

Tracing of feedback fibers
We checked the distribution of cortical feedback fibers originating in the aPCx (+1.7 mm A-P, 2.4 mm M-L, 4.0 mm depth from surface at 0 degrees from the vertical), and AON (+2.25 mm A-P, 1.0 mm M-L, 4.0 mm depth from surface at 0 degrees from the vertical, AON posterior part - AOP), post labeling them using targeted viral injections. For visualization purposes, vGlut1-Cre mice were used such as to minimize spurious labeling of migrating (GABAergic) granule cells (and their neuropil) passing in proximity of AON on the way to the bulb. 100nl of AAV2.9-FLOXED-GFP was injected in the AON or aPCx unilaterally and expression was checked 2 weeks post-infection. 100μm sagittal and coronal bulb slices were obtained after perfusing the brain in PFA. GFP expression was checked under a multiphoton microscope (Figure S3).

Histology
Animals were perfused intra-cardially, the brains preserved in PFA and sliced sagittaly in 100μm thick sections. Slices were mounted on slides using VECTASHIELD Mounting Medium and imaged using an epifluorescence microscope.

Experimental design
For the concentration-series experiments, 16 mice were employed (aPCx saline – 5 mice, 5 FOVs; aPCx muscimol – 5 mice, 5 FOVs; 9 mice for aPCx saline or muscimol; AON saline – 4 mice, 5 FOVs; AON muscimol – 5 mice, 6 FOVs; 7 mice for AON saline or muscimol). In a subset of the aPCx suppression experiments, the same animal was imaged more than once. Two mice (4 FOVs) were injected with saline, as well as muscimol in AON, while allowing at least 3 days of intervening recovery time between injections. Each FOV represents a non-overlapping set of mitral or tufted cells. For the larger-odor panel experiments, 22 animals (8 mice for aPCx; 14 mice for ipsi- and contra-AON experiments) were used. For most experiments, a given brain hemisphere was injected with either saline or muscimol only once. For a subset of experiments (n = 8 mice), both saline and muscimol were injected in the same hemisphere at different times while allowing at least 3 days of intervening recovery time between injections.

QUANTIFICATION AND STATISTICAL ANALYSIS

Pre-processing and detection of significant odor responses
Images were registered laterally (X-Y), and fast Z-movements across individual frames accounted for as previously described (Chae et al., 2019; Otazu et al., 2015). Regions of interest (ROIs, mitral and tufted cell somata) were manually selected based on anatomy performed using custom routines in Matlab. To determine the degree of signal contamination by the neighboring neuropil, in a subset of fields of view, for each ROI, a peri-somatic neuropil annulus (10-20μm from the outer edge of the ROI) was generated. Pixels belonging to neighboring non-neuropil ROIs were not included in the annuli. Fluorescence transients were neuropil-corrected as previously described (Kerlin et al., 2010; Peron et al., 2015) ($F_{ROI-corrected} = F_{ROI} - \alpha F_{neuropil}$). For each ROI, the α parameter was

systematically varied between 0 to 1 in 0.25 increments, and the correlation between neuropil-subtracted and raw fluorescence change signals assessed for both z-scored and non-z-scored data. In the z-scored data, neuropil-subtracted signals matched the raw signals with high correlation (slope ~1) for all α-s considered. In the non-z-scored data, the neuropil-subtracted and raw signals were highly correlated (slope ~1) for $\alpha \leq 0.75$ (recent studies used α values ranging from 0.5 to 0.7; Chen et al., 2013; Kerlin et al., 2010; Khan et al., 2018; Peron et al., 2015). Thus, neighboring neuropil contamination does not appear to significantly change the odor responses of the sampled mitral and tufted cells (Figure S1E). However, given the lack of ground truth for α calling, for the dimensionality reduction and all decoding analyses described in Figures 1, 2, 6, 7, S1, S2, S8, and S9 we used the z-scored data without neuropil subtraction.

To determine significance, for each trial and each ROI, we compared the odor evoked normalized fluorescence with values calculated during the air period preceding odor presentations in the session. For calculating F0, we used the median fluorescence value during the odor period for each trial for each region of interest. Responses that exceeded 99.5 percentile of the air period fluorescence distribution, accumulated across all stimuli and repeats for that ROI, were called significantly enhanced as previously described (Otazu et al., 2015). Responses that were below the 0.5 percentile of the air fluorescence distribution were considered significantly suppressed. An ROI that showed significant responses to an odor in at least two repeats was considered responsive to that odor. Non-significant responses were set to 0 (Figures 3F, 3G, 4A–4C, 5A, 5B, 5D, 5E, S4F, S5, S6B, S6C, S6F–S6I, and S7F–S7H). For the analyses performed in Figures 1, 2, 5C, 5F, 5H, 5I, 6, 7, S1, S2, S7A–S7E, S8, and S9, no thresholding was applied. For Figures 3D, 3E, S4C–S4E, S5, S6A, S6D, and S6E only response pairs significant in at least one condition (pre- or post-) were used.

For investigating whether the changes in the mean response amplitude, number of responses per cell and pairwise odor similarity (Figures 3E, 3G, and 4C) are statistically significant, we used the Wilcoxon sign-rank / rank-sum tests because they are non-parametric and do not assume that the difference between the paired samples is distributed normally. We used the one-sided sign-rank test for the matched samples to explicitly check the hypothesis that the response amplitude increased after muscimol instead of testing whether they are different. For all these comparisons, we further verified that our results are robust and are deemed significant when using a t-test or two-sided versions of the Wilcoxon test as well.

We calculated the signal-to-noise ratio (SNR) of mitral and tufted cell responses as the average signal / standard deviation of signal across individual repeats before and after muscimol suppression of cortical activity. The SNR of mitral and tufted cell responses were comparable (largely overlapping distributions, slightly higher for tufted cell vs. mitral cell ensembles, Figures S1G and S9). Suppressing aPCx or AON activity resulted in increased SNR for both the mitral and tufted cell responses (Median SNR mitral cells post-muscimol = 4.99 vs. 3.25 pre-muscimol; 1,809 cell-odor pairs; Median SNR tufted cells post-muscimol = 7.03 vs. 4.46 pre-muscimol; 2,138 cell-odor pairs), while the decoding performance showed a considerable decrease for the mitral cell based decoders, and to less degree for the tufted cell decoders (Figures 6 and 7).

Odor similarity (odor correlation)

The uncentered odor correlation (odor similarity, $S^{(A,B)}$) was calculated from the population responses vectors of each pair of odors (A, B) in the panel, in each field of view. Cells responsive to least two odors in the panel were included in the similarity analysis.

$$S^{(A,B)} = \frac{\sum_{j=1}^{n} r_j^{(A)} \cdot r_j^{(B)}}{\sqrt{\sum_{j=1}^{n} r_j^{(A)} \cdot r_j^{(A)}} \sqrt{\sum_{j=1}^{n} r_j^{(B)} \cdot r_j^{(B)}}}$$

where r_j^A = response of ROI r_j to odor A, r_j^B = response of ROI r_j to odor B, n = number of ROIs.

Same analysis was also performed using Pearson's correlation, obtaining qualitatively the same results with respect to changes in pairwise odor similarity of mitral versus tufted cell ensembles when suppressing activity in aPCx versus AON (data not shown). We have considered cells responding to at least two odorants, since over time during the imaging sessions responses tend to decrease in amplitude (as observed across repeats in both before-injection and after-saline injections, and as stated in the submitted manuscript). Hence cells which, to begin with, respond to only one odorant would be more likely to be affected by this non-specific decay. We verified that all the changes reported in pairwise odor similarity, response amplitude and number of responses for the mitral vs. tufted cell ensembles upon suppression of the aPCx vs. AON also hold when cells responding to at least one odorant in the panel were included in the analysis.

Correlation between same odor responses across conditions

The uncentered correlation coefficient was calculated from the population cell response vectors for individual odor across conditions (before- vs. after-muscimol / after-saline injection) accumulated across fields of view (Figures 5H, 5I, and S7A–S7D), or for each field of view (Figures 5C and 5F). Cells responsive to least two odorants in the panel were included in the correlation analysis. After-injection responses were scaled down (Figures S7B–S7D) such as to match the mean of their before-injection responses. Cells responsive in both conditions, as determined by identifying significant odor responses, were used calculate the scaling down factor. Cell responses to each odor were scaled down independently. Non-significant responses after-injection were left unchanged.

Neuron
Article

CellPress

Dimensionality reduction (PCA and dPCA)

Extracted ROI time courses were assembled in a data cube (N by S by T) of trial averaged dF/F_0 responses, where N stands for the total number of neurons included, S is the total number of stimuli and T is the total number of time-bins. To reduce the dimensions of the neuronal population, this data cube was re-shaped into a data matrix (N by ST) and normalized (z-scored) such that each stimulus as a function of time represents a point in an N dimensional neural state space. Neural responses were z-scored to avoid biasing the results to differences in absolute values of response magnitude between the two neuronal classes analysed (mitral versus tufted cells). To find a set of orthogonal directions that maximizes the variance captured from the data, we performed principal component analysis (PCA) and identified the *eigen* vectors of the associated covariance matrix. PCA was performed using built-in 'princomp' function in MATLAB. Data projected onto the first three principal components (PCs) is plotted in Figure S1. The variance explained by each PC is given by the ratio of its *eigen* value to the sum of all the *eigen* values.

Demixed PCA, a linear dimensionality reduction technique developed by the Machens group (Kobak et al., 2016) (https://github.com/machenslab/dPCA/tree/master/matlab) was adopted here to decompose the population neural responses into individual components along different features of the odor stimuli. Individual OB output neuron responses multiplex odor identity and concentration representations (Figures 1C–1F). Demixed PCA attempts to linearly un-mix these ensemble representations into certain user-defined components, and reveal the dominant neural activity modes (demixed-PCs). In Figures 1C–1F, the components were odor identity (I) and odor concentration (C). Data projected onto the first three demixed 'identity' PCs or 'concentration' PCs are plotted in Figures 1E and 1F. The same analysis was performed separately for mitral and tufted cells populations. Success in de-mixing odor identity and concentration dimensions implies that a particular linear combination of neurons exists that can 'decode' odor identity with concentration invariance, while, at the same time, a different linear combination of the same neural responses can be used to infer the absolute stimulus concentration, irrespective of the odor identity.

Decoding odor identity (sparse logistic regression and support vector machines)

Odor classification from population neural data was performed using a sparse logistic regression-based decoder with L1 minimization (*lassoglm* function in MATLAB, Figure S8G) and a support vector machine (*fitcsvm* function in MATLAB, Figures 1, 6, 7, S2, S8, and S9) based decoder with either linear or non-linear polynomial kernels. The feature vectors were z-scored mean odor responses for each cell. Decoding accuracy at any time point (in 200 ms bins) was evaluated based on mean neuronal responses from odor onset up to that time point. For example, decoding accuracy at 400 ms takes into account mean neuronal responses from odor onset up to 400 ms. All neurons recorded from multiple field-of-views were pooled, and the number of neurons used in the analyses was varied by sub-sampling (bootstrapping) from this set. The total number of mitral cells (n = 447) and tufted cells (n = 458) were within 2.5% of each other and can be therefore assumed to be approximately 1:1. In all cases, odor classification was analyzed with cross-validation using held-out test dataset. The number of cells considered in the analysis was increased systematically (steps of 5) until all imaged cells were included (Figures 2B and 2E). For each subset of k cells considered, a bootstrap strategy was run 10 times; in each iteration, the decoders were trained and further cross-validated using response from a set of k cells was picked randomly with replacement from all cells. Classification performance as a function of time since odor onset (Figures 2B, 2C, 2E, and 2F) was evaluated for a fixed number of neurons (n = 200). This procedure was performed 10 times, where 200 neurons were randomly sub-sampled from all neurons recorded. Classification performance as a function of neurons (Figures 2B and 2E) was evaluated at a fixed latency from odor onset (t = 1 s). The SVM was not constrained to pick the best among the alternative possibilities, which would have resulted in chance accuracy of 20% for a five-odor stimulus panel. Instead, failure to accurately classify the corresponding odor identity resulted in a chance performance accuracy of zero.

The difference between performance distributions across cell-types or pharmacological manipulations, were quantified in two ways - the sensitivity index equivalent to the d-prime (Figures 2, 6, and S8) and performance difference index (Δ performance, normalized, Figures 6, 7, and S8). Sensitivity index (d-prime), evaluated at each time bin, measured the difference between mean classification performance of the two distributions (m1 and m2) normalized by their standard deviations (σ1 and σ2) as follows:

$$d - prime = \frac{|m1 - m2|}{\sqrt{0.5(\sigma1^2 + \sigma2^2)}}$$

Performance difference index (PDI = Δ performance, normalized) was calculated as:

$$PDI = \frac{(m1 - m2)}{(m1 + m2)}$$

For classification performance comparisons before and after cortical inactivation (Figures 6 and 7), decoders were trained on intact circuit neural responses and then tested using responses from the *same* neurons after inactivation. In Figure S8H, decoders were re-trained after cortical inactivation separately and cross-validated performance was calculated using held-out trial repeats.

Details of the exact type of cross-validation depend on the four different decoding schemes investigated, as described below:

Generalization to novel concentrations

The decoder learned to group any three of four concentrations sampled for a given odorant together. The cross-validated performance was tested on the ability to classify the novel fourth concentration previously not used to train. In Figure 2B, training for

CellPress

Neuron
Article

the lowest two and highest concentrations and testing for the third (second strongest) is shown as example. Figure 2E shows the performance of the decoder in time averaged across all 4 possible combinations of train and test concentrations while varying the number of cells included in the analysis. Our stimulus panel has five odorants each presented at four different concentrations. For example, in the training set, the classifier neuron for Odor 1, should learn to fire (value = 1) each time Odor 1 is presented and not fire (value = 0) for all other stimuli. This corresponds to the top row of the desired objective matrix plotted in Figure 2A. We further tested how well the classifier performs on the held-out concentration. Given that there are five odorants, one may expect that the chance performance is 0.2. However, the classifier is not set up to pick randomly one of the five odorants. Instead, complete failure to identify an odorant results in 0 value performance, while perfect identification corresponds to 1 as explained above. The performance values can, therefore, be interpreted on a scale between 0 and 1.

Odor identification & concentration decoding
Similar to previous schemes, each odorant has a corresponding classifier neuron. However, each classifier neuron was tasked with identifying the presence of the corresponding odorant (non-zero value), and also simultaneously reporting the relative concentration (on a log scale). The cross-validated performance was evaluated on held-out trials (80% training and 20% testing) same as for *odor recognition*. Classification performance was calculated as a correlation of the decoder output with the objective matrix (Figures 2E, 6F, and 6G).

Concentration-invariant odor recognition
Neuronal responses to 20 stimuli – 5 odors across 4 different concentrations were used for this scheme and required the classification of all concentrations of each odor as one odor identity. Thus, 100% success would be achieved if each output classifier neuron corresponding to one odorant fired exactly four times, one for each concentration sampled of that odorant, and did not fire in response to any of the other stimuli (Figure S2). Cross-validated performance was evaluated by training and testing data-sets, which were taken as different (non-overlapping) repeats of the experimental data (for example, train on 3 repeats and test on the 4th). The plotted decoder performance is averaged across all possible combinations. To test whether the performance of the classifier indeed depended on odor concentrations, for Figure S2E, training and testing procedures were identical except concentration labels of each odorant were randomly shuffled for each iteration.

Discrimination across a larger (20) odor set
Ensemble mitral and tufted cell responses to 20 diverse odor stimuli were used for this task. For each odor, we considered one output classifier neuron. In the full task, the decoder learns to call the target odor from all other nineteen stimuli. The number of possible odors included in the analysis was varied systematically from 2 to 20 using bootstrap sub-sampling (n=10). Cross-validated performance was evaluated by training and testing data-sets which were taken as different (non-overlapping) repeats of the experimental data. Performance was plotted as average across all possible combinations, while varying the number of odors included (Figures 7B–7E). Performance difference index (see above) was calculated as a function of the total number of distractor odorants.

Quantifying the effect of cortical feedback suppression
Saline regression was performed using all cell-odor pairs (for both response amplitude and odor similarity analyses) before and after saline injection into ipsi-aPCx or ipsi-AON. Combining all imaged fields of view, a regression line was obtained by minimizing the Euclidian distances from this line to the cell-odor pairs included in the analysis (Figures 3G, 4B, 4C, S4C–S4F, S5B–S5E, S6B, S6C, and S6F–S6I). A 95% percentile confidence interval with respect to the saline regression line was imposed when calculating the significance of muscimol-induced changes in response amplitude or pairwise similarity. For the response amplitude analysis, only cell-odor pairs showing significant responses in at least in one condition (before or after injection) of saline or muscimol were included.

Odor similarity-matching number of mitral cells and tufted cells
To match the number of mitral cells and tufted cells used to construct the population responses vectors, we randomly selected 40 cells per field of view, sampling 4 fields of view of mitral cells and 4 fields of view of tufted cells for each iteration of the bootstrap analysis (100 iterations). Saline regression was performed independently for each iteration using the same number of cells and fields of view, and the effects of muscimol injection computed accordingly (Figures S6D–S6I).

Additional considerations for the decoding analyses
We investigated the performance of mitral and tufted cell based decoders in several decoding schemes inspired from analogous computations necessary for solving olfactory behavioral tasks. When analyzing specific tasks (e.g. *generalization across concentrations* and *odor identification and concentration decoding* schemes, Figures 2A, 2B, versus 2D), we observed differences in performance that were more apparent for the mitral cell-based decoders. Generalizing odor identity to novel concentrations can be thought of as a harder problem than decoding odor identity as well as concentration, since odor responses vary considerably across concentrations, especially when sampling over a range of three orders of magnitude. To correctly identify odorants, the olfactory system (as well as our classifiers) may need to impose additional constraints, i.e. disregard the intra-odorant variations, while learning the

Neuron
Article

CellPress

inter-odor differences. This is indeed reflected in our analyses: classifier performance for Figures 2A and 2B was lower than for Figures 2D–2F. Mitral cell responses are largely non-monotonic and diverse across concentrations of a given odor. Thus, assigning the same value to different concentrations of the same odor (binding them together as one category) may be harder than differentiating across concentrations of the same odor. Compared to mitral cells, tufted cell responses are more monotonic with respect to concentration; this likely makes it easier for odor identification to generalize across different concentrations (Figures 2A–2C). Importantly, in both cases, classifiers based on tufted cell responses performed substantially better than those based on mitral cell responses.

Given that the classifiers employed in these tasks were trained using small number of samples for a given stimulus (∼4 repetitions) and using random sets of neurons sampled across animals, the overall decoding performance of both tufted and mitral cells ensembles reported may represent a lower bound. Further, these observations can be taken as a conservative estimate of the tufted cells' decoding performance, since in our analysis we considered a 1:1 ratio of tufted-to-mitral cells, while recent anatomical reports estimate this ratio to be substantially higher (4:1) (Schwarz et al., 2018).

Technical comments on response strength and its temporal dynamics

We discuss below potential issues in the interpretation of our results obtained via optical imaging of calcium signals related to differences in the signal to noise ratio and the temporal dynamics of mitral versus tufted cell responses.

Signal to noise ratio (SNR)

Suppressing aPCx or AON activity augmented the response amplitude (Figures 3B–3E, S4C–S4E, S6A, S6D, S6E, and S8F) and increased the SNR of both mitral and tufted cell responses (Median SNR mitral cells post-muscimol = 4.99 vs. 3.25 pre-muscimol; 1,809 cell-odor pairs; Median SNR tufted cells post-muscimol = 7.03 vs. 4.46 pre-muscimol; 2,138 cell-odor pairs, Figure S9). However, the decoding performance showed a considerable decrease for the mitral cell based decoders, and to less degree for the tufted cell decoders (Figures 6 and 7). Therefore, an increase in SNR does not necessarily imply a higher decoding accuracy, and SNR differences could not explain the differential effects of cortical feedback suppression on mitral and tufted cell ensembles. Training classifiers separately on the pre- and post- cortical silencing data sets did not change the advantage of tufted-versus-mitral cell decoders (Figure S8H).

Temporal dynamics of responses

Previous work proposed that for decoding odor identity a small number of early responsive glomeruli / second order neurons and their relative timings may be responsible for setting the perceptual qualities of an odor (Chong et al., 2020; Hopfield, 1995; Wilson et al., 2017). We found that subsets of tens of tufted cells randomly picked appear sufficient for fast decoding of odor identity in a concentration invariant manner for conditions where the number of stimuli to discriminate is relatively low (Figures 2 and 6).

Throughout the study, we imaged calcium signals in mitral and tufted cells. These are slower than measuring spike times using electrophysiology methods. We outline below several reasons why this does not impact our main conclusions that tufted cells respond substantially faster compared to mitral cells, and that tufted ensembles outperform mitral cell ensembles at decoding odor identity and intensity all throughout the duration of the odor presentation. *First*, while the calcium signals (as reported by GCaMP3/6f at up to 50Hz sampling rate) are slower to decay (half time ∼250 ms), they are fast (∼10-20 ms) in their onset. This is several times faster than the behavioral response time-scales for odor identification, enabling us to evaluate the decoding performance of neuronal ensembles in the olfactory bulb. *Second*, both mitral and tufted cells showed high (∼95%, Figures 7B and 7C) decoding accuracy, as early as first few hundred milliseconds in the easier versions of the odor discrimination task (e.g. binary odor discrimination) and matched reports of behaviorally performance of mice engaged in olfactory tasks (Abraham et al., 2004; Mathis et al., 2016; Rokni et al., 2014; Uchida and Mainen, 2003; Uchida et al., 2006; Zariwala et al., 2013). This would be impossible if the temporal resolution of our experimental technique were limiting. The differences we report between the decoding performance of the mitral and tufted cell ensembles became more pronounced with increasing the task difficulty (Figures 1, 2, 6, and 7). *Third*, two photon imaging of GCaMP signals afforded the temporal resolution for distinguishing between the fast responding tufted versus the lagging mitral cells (Figure S1C). In our experiments, tufted cells were generally more proficient than mitral cells at decoding odor identity and/or concentration. This occurred not only as early as a few hundreds of milliseconds from odor onset (Figures 2, 6, and 7), but all throughout the odor period. Our observations are consistent with whole-cell and cell attached millisecond-resolution recordings showing that tufted cells are faster than mitral cells (response latency ∼100ms vs. 300ms; Igarashi et al., 2012), stronger in response amplitude (Fukunaga et al., 2012; Igarashi et al., 2012; Jordan et al., 2018; Nagayama et al., 2004) and more reliably driven by olfactory sensory neuron input (Gire et al., 2012). The results reported here bring new insight by quantifying, across many cells and several odor decoding schemes, the ability of tufted cell ensembles to represent both odor identity and intensity over a wide range of concentrations. They were enabled by multiphoton imaging which affords substantially higher yield compared to whole-cell recordings and distinguishes between mitral and tufted cells (Chae et al., 2019; Kapoor et al., 2016; Kato et al., 2012; Kikuta et al., 2013; Otazu et al., 2015; Yamada et al., 2017). Further investigation is nonetheless required to elucidate potential differences between tufted and mitral cell ensemble representations with spike-time resolution.